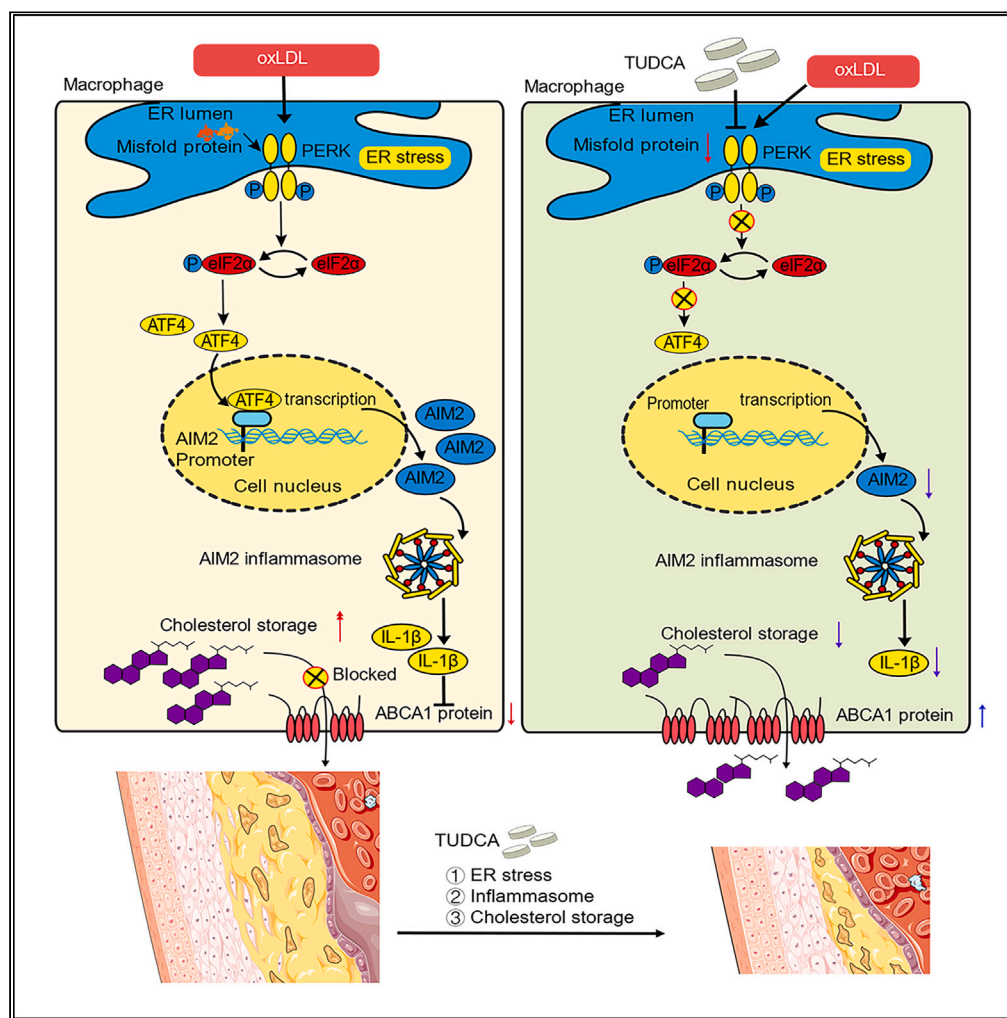**Article**

TUDCA alleviates atherosclerosis by inhibiting AIM2 inflammasome and enhancing cholesterol efflux capacity in macrophage

Xuyang Wang,
Yuesheng Zhang,
Luping Du, ...,
Yijiang Zhou,
Xiang Yin,
Xiaogang Guo

gxg22222@zju.edu.cn

Highlights

TUDCA alleviated atherosclerosis and promoted cholesterol efflux capacity of macrophages

TUDCA inhibited activation of the PERK/eIF2α/ATF4 and AIM2 inflammasome

ATF4 affected transcriptional activity of AIM2

AIM2 mediated foam cell formation by targeting ABCA1

Article

TUDCA alleviates atherosclerosis by inhibiting AIM2 inflammasome and enhancing cholesterol efflux capacity in macrophage

Xuyang Wang,[1,3] Yuesheng Zhang,[1,3] Luping Du,[1,3] Zhengchen Jiang,[2] Yan Guo,[1] Kai Wang,[1] Yijiang Zhou,[1] Xiang Yin,[1] and Xiaogang Guo[1,4,*]

SUMMARY

Cholesterol efflux capacity (CEC) dysfunction in macrophages is important in atherosclerosis. However, the mechanism underlying CEC dysfunction remains unclear. We described the characteristics of ATF4 and inflammasome activation in macrophages during atherosclerosis through scRNA sequencing analysis. Then model of hyperlipemia was established in ApoE$^{-/-}$ mice; some were treated with tauroursodeoxy-cholic acid (TUDCA). TUDCA decreased the ATF4, Hspa, and inflammasome activation, reduced plaque area of the artery, and promoted CEC in macrophages. Furthermore, TUDCA abolished oxLDL-induced foam cell formation by inhibiting activation of the PERK/eIF2α/ATF4 and AIM2 inflammasome in macrophages. Further assays revealed ATF4 binding to AIM2 promoter, promoting its transcriptional activity significantly. Then we discovered that ATF4 affected AIM2-mediated foam cell formation by targeting ABCA1, which could be blocked by TUDCA. Our study demonstrated that TUDCA alleviates atherosclerosis by inhibiting AIM2 inflammasome and enhancing CEC of macrophage, which provided possibilities for the development of therapies.

INTRODUCTION

Atherosclerosis (AS) is a major cause of many cardiovascular diseases, such as myocardial infarction and stroke.[1,2] It is a chronic sterile inflammation process within the arteries characterized at the early stage by cholesterol crystal deposition, foam cell formation, and increased extracellular matrix and fibrotic cap development, leading to plaque formation.[3–5] At the early stage, AS is characterized by the endothelial cell (EC) dysfunction and accumulation of lipid-laden macrophages in the vascular wall.[6,7] After EC dysfunction, circulatory macrophages are recruited and infiltrate locally injured arteries, resulting in the development of foam cells.[2,8,9] Cholesterol efflux capacity dysfunction driven by decreased levels of ATP-binding cassette subfamily A member 1 (ABCA1) and ATP-binding cassette subfamily G member 1 (ABCG1) in macrophage cells enhanced the process of foam cell formation.[10] In addition, inflammatory macrophages can perform a series of different functions that control atherosclerotic lesion development.[11–13] Thus, preventing the transformation of macrophages into foam cells should be helpful in alleviating atherosclerosis.

Immune cell reactions and inflammation activation are important processes in the advanced stages of atherosclerosis and myocardial fibrosis after myocardial infarction.[14,15] As the immune cells play a central role in atherosclerosis, macrophages can be activated when treated by oxidized low-density lipoprotein (oxLDL) and secrete multiple cytokines and growth factors, which accelerate cell death and plaque rupture.[16] Both absent in melanoma 2 (AIM2) and NLR family pyrin domain containing 3 (NLRP3) inflammasomes participate in activating inter-leukin-1β (IL-1β) and promote the development of atherosclerosis.[17,18] Notably, deficient expression of ABCA1 and ABCG1 promotes the activation of NLRP3 inflammasomes in myeloid cells (macrophage and monocytes), indicating that cholesterol efflux pathways normally exert anti-inflammatory and anti-atherogenic effects by suppressing inflammation and inflammasome activation in macrophages.[19,20] Moreover, the NLRP3 inhibitor MCC950 ameliorates cell damage by suppressing lipid accumulation by increasing the ABCA1 expression and decreasing the sterol regulatory element-binding protein 1 (SREBP1) and sterol regulatory element-binding protein 2 (SREBP2) expression.[21] These findings indicated a comprehensive relationship between inflammasome and cholesterol storage. Although one study found that oxysterol restraint of cholesterol synthesis prevents AIM2 inflammasome activation,[22] little is known about the precise link between the AIM2 inflammasome and cholesterol efflux or the effect of cholesterol storage mediated by ABCA1 on AIM2 inflammasome activation in atherosclerosis.

---

[1]Department of Cardiology, the First Affiliated Hospital, Zhejiang University School of Medicine, Hangzhou 310003, China
[2]Department of Gastric Surgery, The Cancer Hospital of the University of Chinese Academy of Sciences (Zhejiang Cancer Hospital), Institutes of Basic Medicine and Cancer (IBMC), Chinese Academy of Sciences, Hangzhou 310022, China
[3]These authors contributed equally
[4]Lead contact
*Correspondence: gxg22222@zju.edu.cn
https://doi.org/10.1016/j.isci.2024.109849

Endoplasmic reticulum (ER) stress is characterized by the unfolded protein response, which is triggered by the accumulation of unfolded and misfolded proteins in the ER, and promotes oxidative stress, impairs calcium homeostasis, and increases the expression of normal proteins.[23] ER stress involves three membrane-associated sensors. One of these sensors is protein kinase RNA-like ER kinase (PERK; also known as Eif2ak3), which oligomerizes and phosphorylates α-subunit of the eukaryotic elongation factor 2 (eIF2a, also known as EIF2S1), attenuating cellular protein synthesis and preferentially promoting translation of activating transcription factor 4 (ATF4).[24,25]

As a conjugated bile acid, tauroursodeoxycholic acid (TUDCA) protects cells from endoplasmic reticulum stress and is responsible for attenuating fibrosis levels and decreasing keloid formation.[26] In a pressure-overload-induced cardiac remodeling model, oral administration of TUDCA alleviated myocardial fibrosis, collagen deposition, and cardiomyocyte apoptosis by reducing ER stress.[27] However, the potential mechanism of ER stress in atherosclerosis and the function of the ER stress inhibitor TUDCA on macrophages is still unclear. Thus, in this study, we investigated the role of ER stress and expounded the partial mechanism or links between ER stress, inflammasome activation, and foam cell formation in atherosclerosis, as well as analyzed the specific function of TUDCA in the progression of atherosclerosis.

RESULTS

High-fat diet promotes ATF4-mediated endoplasmic reticulum stress and inflammasome activation

To delineate the heterogeneity of mouse aortic macrophages during atherosclerosis development, we collected scRNA-seq datasets, which included total CD45$^+$ leukocytes from the aortas of male low-density-lipoprotein-receptor-deficient (Ldlr$^{-/-}$) mice fed a chow (Control) diet, high-fat diet (HFD) for 11 weeks, and HFD for 20 weeks from the public repository (GSE97310). We obtained single-cell transcriptomes for 2,214 cells by integrating three groups from the datasets (Control, 384 cells; HFD 11W, 924 cells; HFD 20W, 906 cells) after strict quality control filters, and graph-based clustering was performed to group these cells according to their respective gene-expression profiles using the t-distributed stochastic neighbor embedding (t-SNE) plots (Figure 1A). We defined five major cell types, which included macrophages (Adgre1, Cd68), lymphocyte lineages (Cd3d, Cd79a, NKG7), neutrophil cells (S100a8), mast cells (Il1rl1), and MoDC/DC (Cd209a, Flt3) based on the established canonical markers[11,28,29] (Figures 1B, S1A, and S1B). Altogether, compared to the control group, we found that the proportion of macrophages increased in total CD45$^+$ cells during the atherosclerosis development (Control, 17.71%; HFD 11W, 45.13%; HFD 20W, 67.44%) (Figure 1C).

Given this situation, we then performed scRNA-seq in all macrophages and further clarified the potential functional heterogeneity of macrophages in the aortas during the development of atherosclerosis (Figure S1C). Notably, through the Gene Ontology (GO) term analyses of macrophages among the three groups, macrophages from HFD groups (HFD 20W) seemed to be enriched for a particular set of functions not found in the macrophages of the control group, such as protein folding, response to interferon-gamma (Figure S1D). What's more, Kyoto encyclopedia of genes and genome (KEGG) analyses also indicated that macrophages from one of the HFD groups (HDF_11W) seemed enriched for a particular set of functions compared with the control group, including protein processing in endoplasmic reticulum (Figures 1D and S1E). Additionally, the expression of genes associated with ER stress genes (Eif2ak3, Eif2s1, and ATF4) and inflammasome-related genes (Aim2, Gasdermin d [Gsdmd], and Il1b) in the HFD groups also increased significantly compared with the control group (Figure 1E).

As ATF4 is the final factor of PERK/eIF2a/ATF4 axis that could influence the transcriptional activity of multiples mRNA,[30] to clarify whether macrophages with high ATF4 levels presented with more severe inflammasome activation, we separated macrophages into subclusters of high expression and low expression of ATF4. Notably, expression of inflammasome related genes including Il1b,Gsdmd, and AIM2 increased in macrophages with high ATF4 expression (Atf4-High) compared to those with low ATF4 expression (Atf4-Low); also, the ER stress gene Eif2s1 was higher expressed in the group of high ATF4-expressed macrophages (Figure 1F). GO analysis also showed that ATF4-high macrophages were enriched for a particular set of functions compared with ATF4-Low macrophages, such as cellular response to unfolded protein and positive regulation of inflammatory response (Figure S1F).

Macrophages in apolipoprotein-E-deficient mice and human atherosclerotic carotid arteries display high levels of endoplasmic reticulum stress and inflammatory response

To further validate our findings in human atherosclerotic plaque, we examined the expression of PERK, eIF2a, ATF4, AIM2, and IL-1β from the published microarray data of human carotid plaques from 32 patients (GSE43292). We found that the expression levels of PERK, Eif2S1, AIM2, NLRP3, and IL-1β increased significantly in the carotid plaques and presented the positive correlation between PERK and AIM2 inflammasome activation (Figures 2A and S2A). To further evaluate the level and location of ATF4 in human plaque, human carotid atherosclerotic plaques were obtained and the ATF4 expression was measured by immunochemistry. Interestingly, although there was a high-level colocation of ATF4 with SM22$^+$ cells in the healthy artery, there is excessive ATF4 accumulated in the area of CD68$^+$ cells in the advanced stage of atherosclerosis (necrotic core formation and plaque rupture) (Figures 2B and S2B). We then selected macrophages from the original scRNA-seq dataset of human atherosclerotic carotid arteries (n = 1,714 cells, GSE155514) (Figures 2C and S2C). Consistent with the analysis results in mice, these macrophage subpopulations also expressed genes associated with ER stress (EIF2A, EIF2S1, and ATF4) and inflammasomes (Gsdmd, IL1B, and IL18) (Figure 2D). Additionally, GO analysis of macrophage subclusters revealed that the whole four subclusters were enriched for a particular set of functions such as ERK cascade, protein targeting to endoplasmic reticulum, protein localization to endoplasmic reticulum, and establishment of protein localization to endoplasmic reticulum (Figures 2E and Figure S1G).
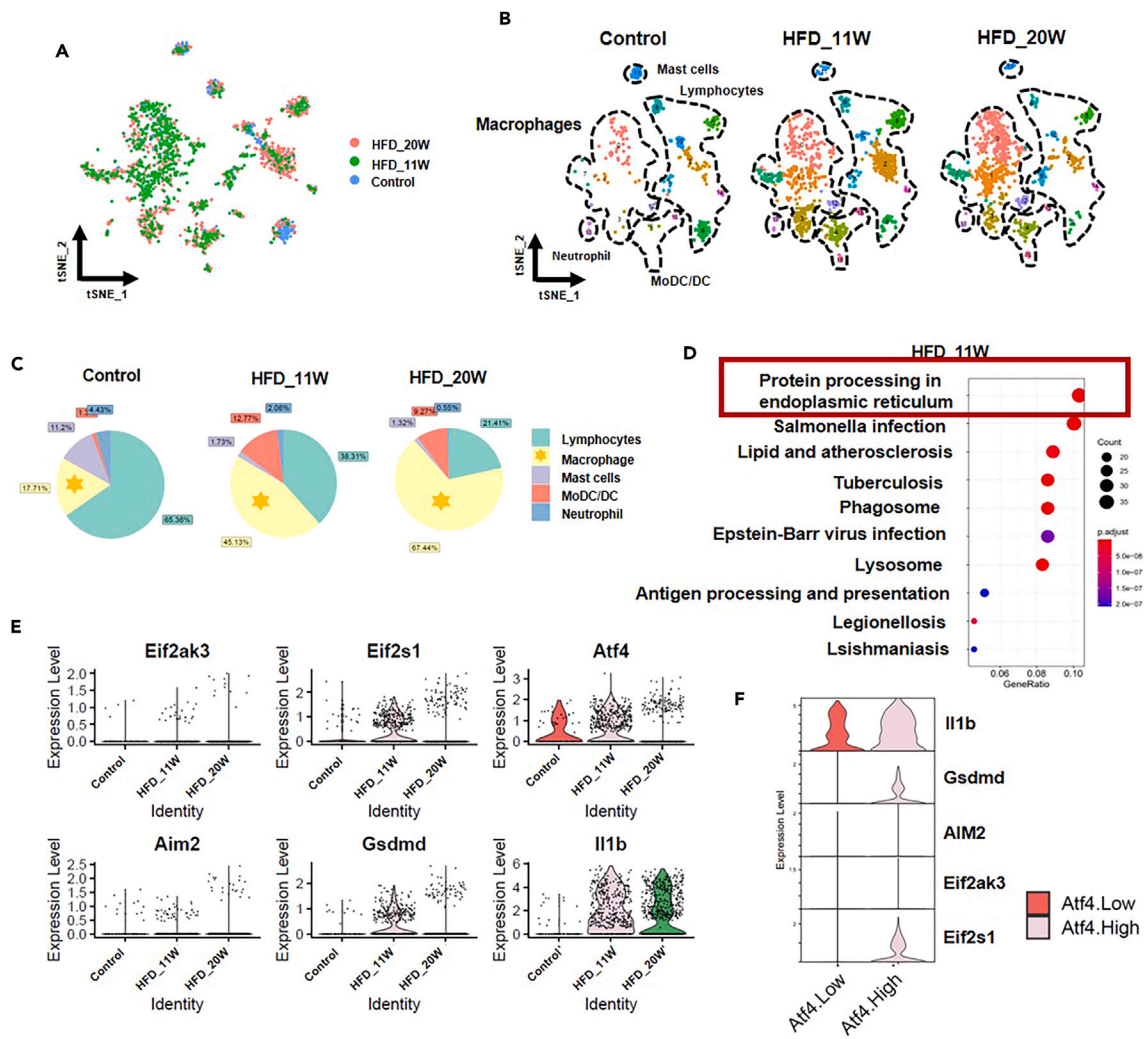
Figure 1. High-fat diet increased ATF4-mediated ER stress and inflammasome activation in atherosclerotic macrophages

(A and B) TSNE plot displaying the major cell types and color-coded cell clusters among Control, HFD_11W, and HFD_20W group.

(C) Pie plot showing the percentage of major cell types among different datasets at different stages of atherosclerosis.

(D) KEGG analysis displaying the related pathways of Control and HFD_11W group.

(E) Violin plot showing the expression of endoplasmic reticulum stress markers (Eif2ak3, Eif2s1, and Atf4) and inflammasome markers (Aim2, Gsdmd, and Il1b) of all macrophages among three groups.

(F) Violin plot showing the expression of selected marker genes (AIM2, gsdmd, Il1b, Eif2ak3, Eif2s1) between Atf4.High and Atf4.Low group in all macrophages.

Inhibition of ER stress alleviates plaque formation and lipid accumulation in Apoe−/− mice fed a high-fat diet

To examine whether the inhibition of ER stress influences plaque formation and lipid accumulation in the HFD-induced Apoe$^{-/-}$ mice, TUDCA (1,000 mg/kg/day) was administered to HFD-induced Apoe$^{-/-}$ mice (Figure 3A). After 4 weeks of TUDCA treatment, TUDCA treatment did not influence the levels of blood lipids such as total cholesterol, total triglyceride, and low-density lipoprotein (LDL) (Figures 3B–3E) and the body weight of mice (Figure 3F). Lesion area (Oil red O positively [ORO$^+$] stained area) of the whole aorta decreased significantly compared with that in the untreated HFD group (Figure 3G). To evaluate plaque burden in the aortic sinus, H&E, ORO, and Masson staining were performed on consecutive sections (Figure 3H). The lesion area increased significantly in the aortic sinuses of mice fed the HFD. Additionally, TUDCA treatment decreased plaque lesions compared to mice administered a saline treatment. Masson staining indicated that plaque stability increased significantly in HFD Apoe$^{-/-}$ mice, and TUDCA treatment alleviated the high proportion of the ORO$^+$ area and increased the fibrotic cap of the plaque (Figure 3H). As macrophages, vascular smooth muscle cells, and ECs are known to be the major cell populations in atherosclerotic plaques, we performed an immunochemistry analysis to measure their abundance. Using this analysis on consecutive sections, we found abundant expression of monoclonal antibody Moma-2, which is specific to macrophages and monocytes, in HFD-induced atherosclerotic lesions, though TUDCA treatment reduced the number of macrophages in the lesions even with the HFD,
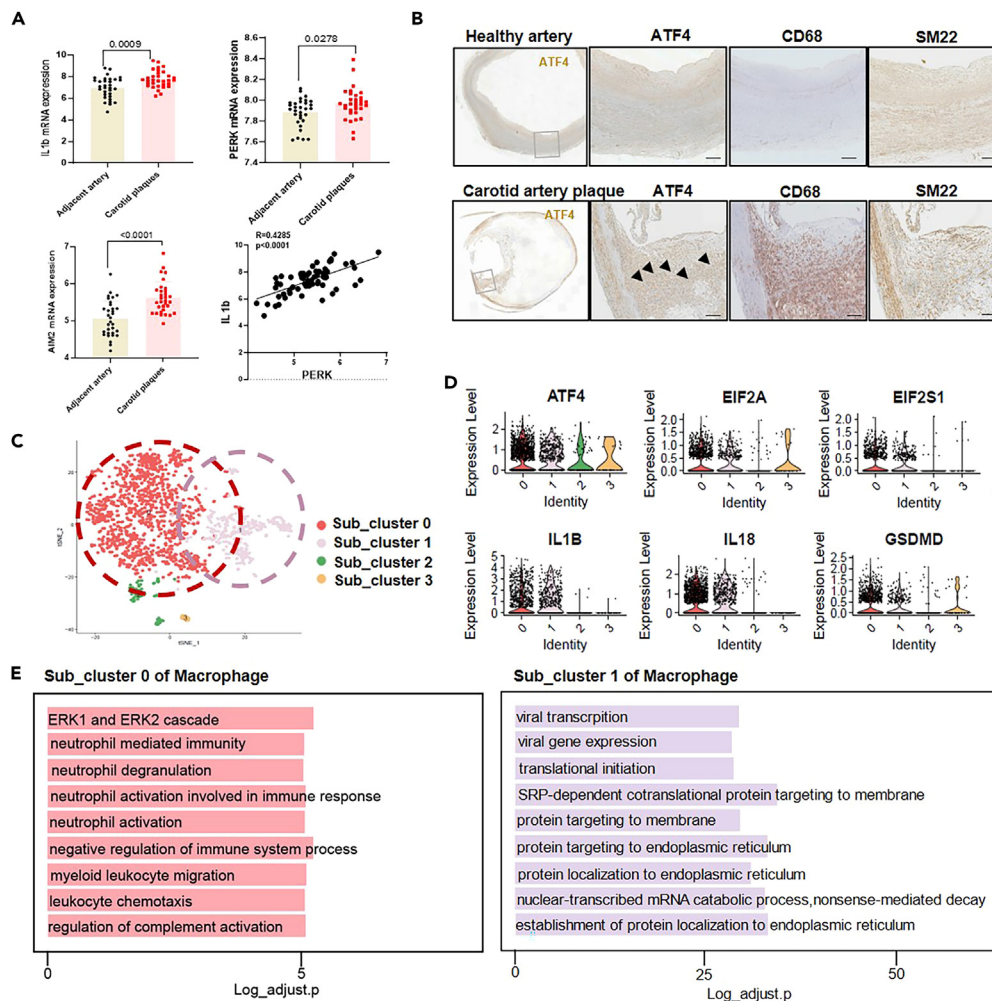
Figure 2. Macrophages in ApoE$^{-/-}$ mice and human atherosclerotic carotid arteries show high level of ER stress and inflammatory response

(A) The relative mRNA expression levels of IL1b, PERK, and AIM2 between adjacent artery and carotid plaques and linear regression analysis of IL1b and PERK.

(B) Immunohistochemical staining of selected markers (ATF4, CD68, and SM22) between healthy artery and carotid artery plaque. Scale bars: 200 μm.

(C) TSNE plot displaying distribution of macrophage subpopulations of human atherosclerotic carotid arteries.

(D) Violin plot showing the expression of endoplasmic reticulum stress markers (Eif2a, Eif2s1, and Atf4) and inflammasome markers (Il1b, Il18, and Gsdmd) of all macrophages.

(E) Bar plot showing the Gene Ontology (GO) enrichment of cluster 0 and cluster 1.

whereas the alpha smooth muscle actin (αSMA), which is specific to smooth muscle cells, did not reduce significantly though TUDCA treatment (Figure 3I).

TUDCA alleviates ATF4-mediated ER stress, inflammasome activation, and cholesterol efflux of macrophages in ApoE$^{-/-}$ mice fed a high-fat diet

To investigate transcription differentiation among Apoe$^{-/-}$ mice fed a normal-fat diet (NFD), the HFD, or the HFD with TUDCA treatment, bulk RNA-seq of the whole artery was performed (Figure 4A). Principal-component analysis demonstrated that there were different transcription spaces under different intervention conditions among the three groups (Figure 4B), and the heatmap also showed the correlation of the samples of NFD group, HFD group, and HFD_TUDCA group (Figure S3B). Venn diagram showed all different genes among the three groups (Figure S3A). Besides, differentially expressed genes (DEGs) were analyzed using DESeq2 software between the two groups; there were 988 DEGs between the NFD group and HFD group and 245 DEGs between the HFD and HFD+TUDCA groups (Figure S3C). Heatmap of the NFD, HFD, and HFD+TUDCA groups showed the characteristics of DEGs among these three groups: there was significantly high expression of matrix metalloproteinase family (MMP9, MMP25, MMP8, MMP12, MMP13, and MMP3), CD68, inflammasome (IL1b, IL18bp, ifi44, ifi204, and Nlrp3), ER stress (Hspa5), and cholesterol transporters (ABCA1 and ABCG1) in the HFD group compared with the NFD group; however,
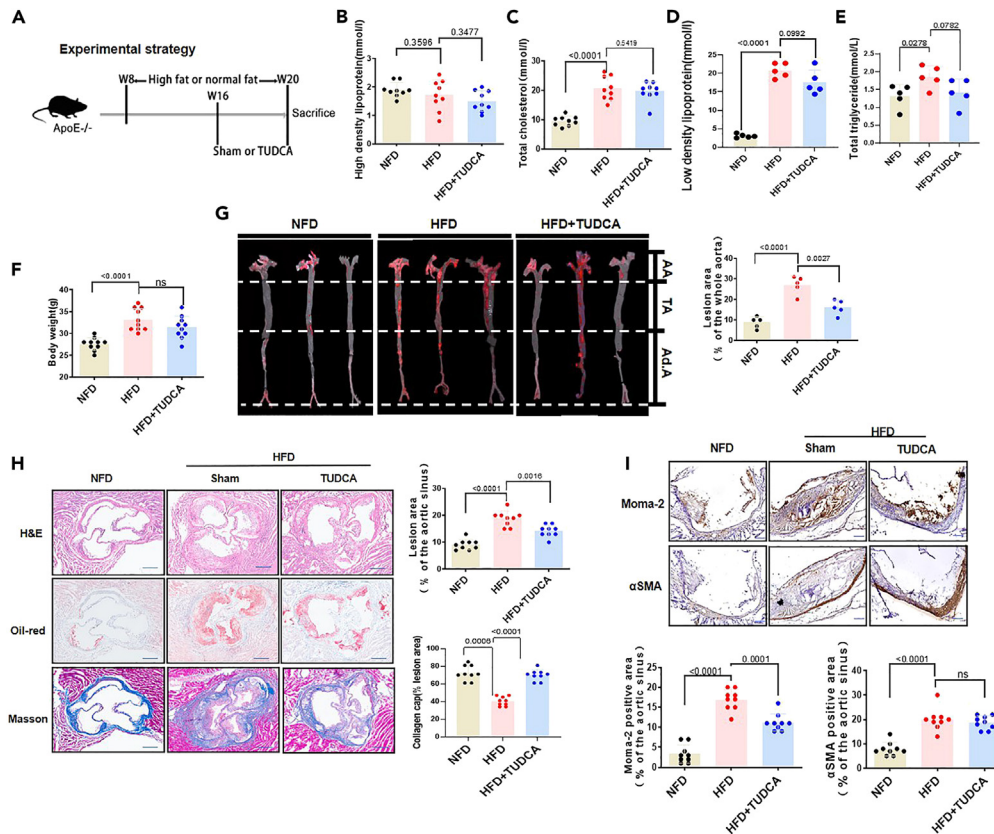
Figure 3. TUDCA alleviate plaque formation in high-diet-induced atherosclerosis

(A) Experimental strategy of high-diet feed and TUDCA treatment.

(B–E) Plasma total cholesterol ($n = 9$), low-density lipoprotein-cholesterol (LDL-c) ($n = 9$), high-density lipoprotein-cholesterol (HDL-c) ($n = 5$), and triglyceride ($n = 5$); t test. Data are represented as mean $\pm$ SD.

(F) Body weight of per mice ($n = 10$); t test. Data are represented as mean $\pm$ SD.

(G) Oil-red staining of the whole artery among three group and ORO$^+$ lesion area in the whole artery ($n = 5$); t test. Data are represented as mean $\pm$ SD.

(H) HE staining, oil-red staining, and Masson staining of the aortic sinus. Lesion area calculated by the ORO$^+$ lesion area ($n = 9$). Collagen cap area of the plaque was calculated by the Masson staining ($n = 9$); t test. Data are represented as mean $\pm$ SD. Scale bars: 200 μm.

(I) Immunochemistry staining of the Moma-2 and α-SMA of the aortic sinus ($n = 9$). Moma-2-positive area and α-SMA-positive area of the aortic sinus ($n = 9$); t test. Data are represented as mean $\pm$ SD. Scale bars: 40 μm.

TUDCA rescued the high expression of the abovementioned DEGs to different degrees (Figure 4C). Volcano plot showed the up and down genes of the HFD vs. HFD+TUDCA group or of the NFD vs. HFD group (Figures 4D and S3D). As shown by the expression levels of ifi204, Nlrp3, Il1b, and Il18, inflammasome activation was evident in the arteries of the HFD group compared to the NFD group (Figure S3D). The ER stress inhibitor TUDCA not only decreased expression of the ER-stress-related gene Hspa5 but also down-regulated inflammasome activation (as seen with the expression levels of ifi204, ifi44, NLRP3, and IL1b) in the artery of TUDCA-treated mice compared with mice without drugs (Figure 4D). Western blot (NLRP3, IL-1β, and Hspa5) and qPCR (Hspa5, ifi204, ifi44, NLRP3, and IL1b) of the artery in the group of HFD and HFD+TUDCA were performed, and it revealed the same results consistent with the bulk sequencing (Figures 4E and 4F). GO analysis showed that the HFD group was enriched for a particular set of functions compared with the HFD+TUDCA group, including the immune response and inflammatory response (Figure 4G). KEGG pathway analysis also demonstrated that the enriched pathways were mainly related to the immune system, infectious disease, folding, and degradation (Figure S3E). To further investigate ER stress levels, qPCR and western blot analysis of the whole artery were performed. The PERK/eIF2a/ATF4 axis was activated by the high-fat diet in the artery of ApoE$^{-/-}$ mice but TUDCA blocked this effect (Figures 4H, S3F, and S3G). To verify the colocalization of ATF4 in macrophage and smooth muscle cell, immunofluorescence analysis of ATF4, CD68, and α-SMA was performed in the aortic sinus of mice (Figure 4I). This analysis showed that at low plaque burden levels in the mice fed with normal-fat diet, ATF4 was mainly expressed in smooth muscle cells. While macrophages assembled in the necrotic core of the plaque, ATF4 expression increased significantly in the lesion and colocalized with these macrophages. TUDCA decreased the expression of the ATF4 in the macrophages (Figure 4I). To assess the cholesterol efflux capacity of the circulatory macrophages, macrophages radioactively labeled with [^{3}H]-cholesterol (5×10^6 cells/mouse) were injected into these three groups, and the
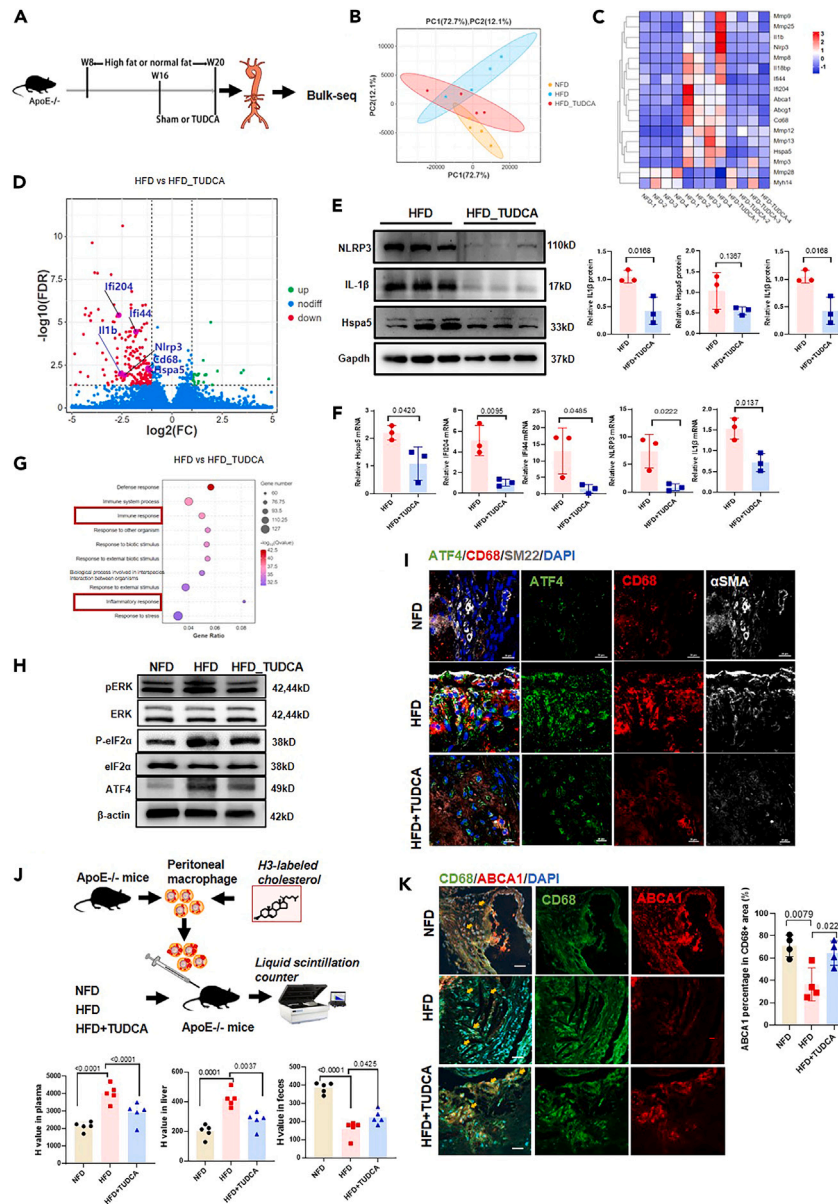
Figure 4. TUDCA alleviates endoplasmic reticulum stress and cholesterol efflux in high-diet-induced atherosclerosis

(A) Experimental strategy of bulk sequencing of the whole artery of ApoE$^{-/-}$ mice with high-diet feed and TUDCA treatment.

(B) Principal-component analysis (PCA) of transcriptomes among three group.

(C) Heatmap showed part of the differentially expressed genes (DEGs) among the NFD group, HFD group, and HFD_TUDCA group (FDR below 0.05 and absolute fold change ≥ 2).

(D) Volcano plot of the up and down genes between HFD group and HFD+TUDCA group (FDR below 0.05 and absolute fold change ≥ 2).

(E) Western blot (NLRP3, IL-1β, and Hspa5) and relative protein ratio of the artery in the group of HFD and the group of HFD+TUDCA (n = 3).

(F) qPCR (Hspa5, ifi204, ifi44, NLRP3, and IL1b) of the artery in the group of HFD and the group of HFD+TUDCA (n = 3).

(G) GO analysis displaying the related pathways of DEGs between HFD group and HFD_TUDCA group.

(H) Western blot analysis of the protein expression of pERK, ERK, pEIF2α, EIF2α, and ATF4 in the artery of mice (n = 5).

(I) Immunofluorescent staining of the ATF4, CD68, and αSMA in the sections of aortic sinus. Scale bars: 20 μm.

(J) Experimental strategy of [3H]-cholesterol efflux capacity in macrophage and the H value in plasma, liver, and feces (n = 5).

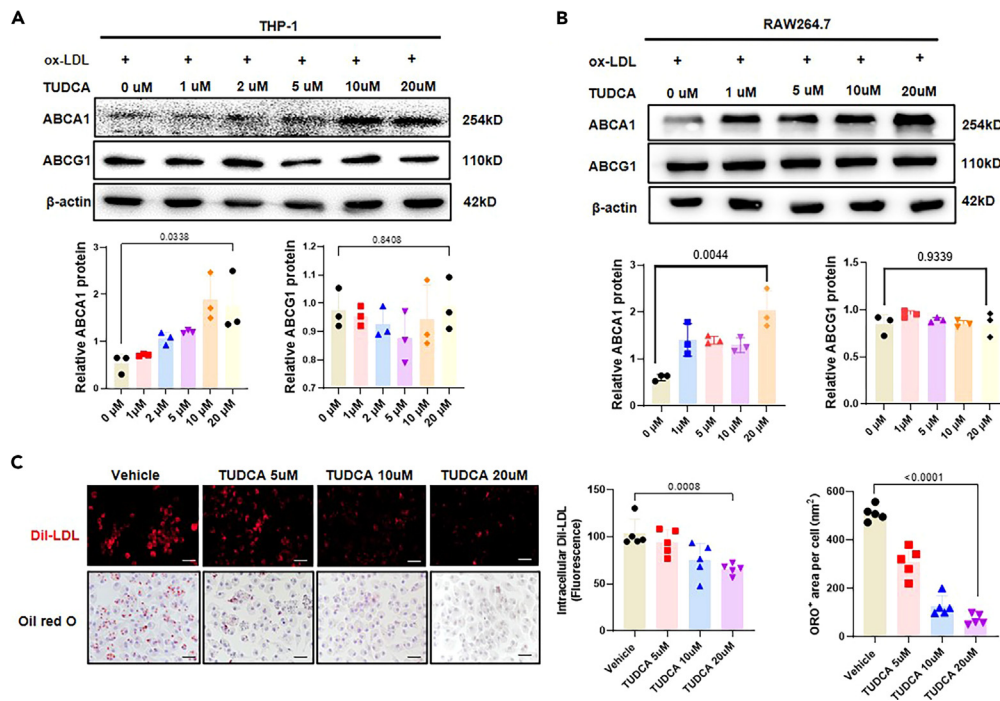(K) Immunofluorescent staining of the ABCA1 and CD68 in the sections of aortic sinus. Scale bars: 20 μm.

Figure 5. TUDCA alleviates lipid storage in macrophage

(A) Western blot analysis of the protein expression of ABCA1 and ABCG1 in different TUDCA treatment concentration in THP1 macrophage with oxLDL stimulation (*n* = 5); t test. Data are represented as mean ± SD.

(B) Western blot analysis of the protein expression of ABCA1 and ABCG1 in different TUDCA treatment concentration in RAW264.7 macrophage with oxLDL stimulation (*n* = 5); t test. Data are represented as mean ± SD.

(C) Dil-LDL and oil-red staining of RAW264.7 macrophage. t test. Data are represented as mean ± SD, Scale bars: 10 μm.

radioactivity level in the plasma, liver, and feces showed that circulatory macrophages in the high-fat diet mice had a low cholesterol efflux capacity; TUDCA treatment increased this capacity, with there being higher H values in feces and lower H values in plasma and liver (Figure 4J). Notably, TUDCA treatment reduced the lipid storage in the liver of HFD mice (Figure S3H). Immunofluorescent staining of CD68 and ABCA1 showed that ABCA1 expression in the CD68$^+$ area increased in the TUDCA treated group (Figure 4K).

TUDCA increases cholesterol efflux capacity in macrophages in a concentration-dependent manner

TUDCA alleviates the inflammatory response and cholesterol efflux capacity of macrophages *in vivo*. To investigate whether TUDCA protects macrophages from cholesterol storage *in vitro*, human THP-1 macrophages were treated with TUDCA at different concentrations (1, 2, 5, 10, and 20 μM). ABCA1 expression increased significantly in THP-1 macrophages in a concentration-dependent manner when stimulated by oxLDL (50 μg/mL) (Figure 5A). Consistent with the results in THP-1 macrophages, the expression of ABCA1 increased significantly in RAW264.7 macrophages as TUDCA concentration increased (1, 5, 10, and 20 μM) when stimulated by oxLDL (50 μg/mL) (Figure 5B). Using a Dil-LDL assay to assess LDL capacity and ORO staining to assess lipid accumulation, we found that TUDCA treatment decreased lipid storage and accumulation of LDL in macrophages (Figure 5C). As TUDCA (10 μM) treatment reduced the ABCA1 expression and lipid storage significantly in macrophages, we selected TUDCA (10 μM) as a suitable concentration for subsequent experiments.

TUDCA reduces oxLDL-induced foam cell formation and PERK/eIF2a/ATF4 activation in macrophages

As oxLDL stimulation promotes foam cell formation of macrophages, 10-μM TUDCA was administered to RAW264.7 macrophages for 24 h following stimulation with 50 μg/mL oxLDL for 24 h. The mRNA and protein expression levels of cholesterol transmembrane transporters, including ABCA1 and ABCG1, were assessed. We found that 50 μg/mL oxLDL significantly inhibited ABCA1 and ABCG1 expression, and TUDCA blocked this effect and significantly increased ABCA1 mRNA and protein expression (Figures 6A–6C). Dil-LDL and ORO$^+$ staining showed that oxLDL stimulation promoted lipid storage in macrophages and that TUDCA both decreased lipid storage and protected macrophages from foam cell formation (Figures 6D and 6E). Activation via phosphorylation of the PERK/eIF2a/ATF4 axis and the protein levels of its components increased after oxLDL stimulation, though TUDCA partly blocked the effect of oxLDL (Figures 6F and 6G). The mRNA expression of the ER stress sensors ATF4, ATF6, and NF-kB increased after oxLDL stimulation, whereas TUDCA decreased their mRNA levels (Figure 6H). Moreover, LY2828360, a slowly signaling G-protein-biased cannabinoid CB(2) receptor agonist, was further used to activate the
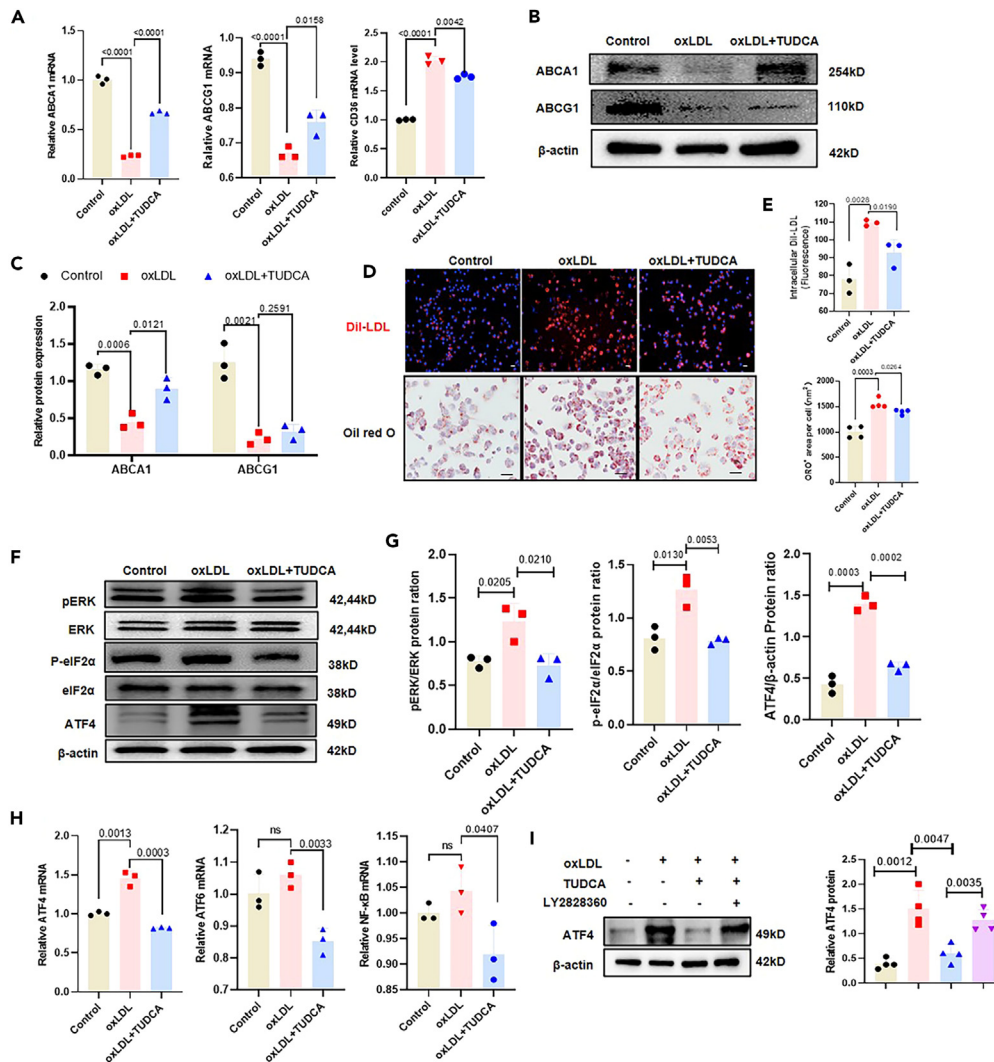
Figure 6. TUDCA alleviates foam cell formation and endoplasmic reticulum stress in oxLDL-induced macrophage

(A) Relative mRNA of ABCA1, ABCG1, and CD36 were detected by RT-qPCR (*n* = 3); t test. Data are represented as mean ± SD.

(B and C) the expression of ABCA1 and ABCG1 were detected by western blot (*n* = 3); t test. Data are represented as mean ± SD.

(D and E) RAW264.7 cells were stimulated with oxLDL; lipid storage was calculated by Dil-LDL staining and oil red O staining (*n* = 3); t test. Data are represented as mean ± SD. Scale bars: 10 μm.

(F and G) The expression of pERK, ERK, pEIF2α, EIF2α, and ATF4 were detected by western blot (*n* = 3); t test. Data are represented as mean ± SD.

(H) Relative mRNA of ATF4, ATF6, and NF-κB were detected by RT-qPCR (*n* = 3); t test. Data are represented as mean ± SD.

(I) The expression of ATF4 was detected by western blot after TUDCA and LY2828360 treatment (*n* = 4); t test. Data are represented as mean ± SD.

ERK1/2 before TUDCA treatment, it showed that the inhibition role on the ATF4 of TUDCA treatment was blocked after the ERK signal activation (Figure 6I).

TUDCA decreases AIM2 inflammasome activation in oxLDL-treated macrophages by targeting ATF4 axis

As previously mentioned, we found that macrophages suffered from inflammasome activation in the plaques of humans and mice, and TUDCA decreased the expression level of inflammasome markers in artery of mice. Heatmap and Volcano plot displayed the differentially expressed genes (DEGs) between the control group and oxLDL group in RAW264.7 macrophages (Figure S4A). In addition, GO analysis showed that the group of RAW264.7 macrophages with oxLDL stimulation enriched for a particular set of functions including the double-strand DNA binding, inflammatory response, and cytosolic DNA-sensing pathway (Figure S4B). It has been demonstrated that AIM2 is a cytoplasmic sensor that recognizes the double-strand DNA in cytoplasm and then activates in cells. To investigate whether TUDCA inhibits AIM2 inflammasome activation and decreases the IL-1β-mediated inflammation, we assessed mRNA and protein levels of inflammasomes in
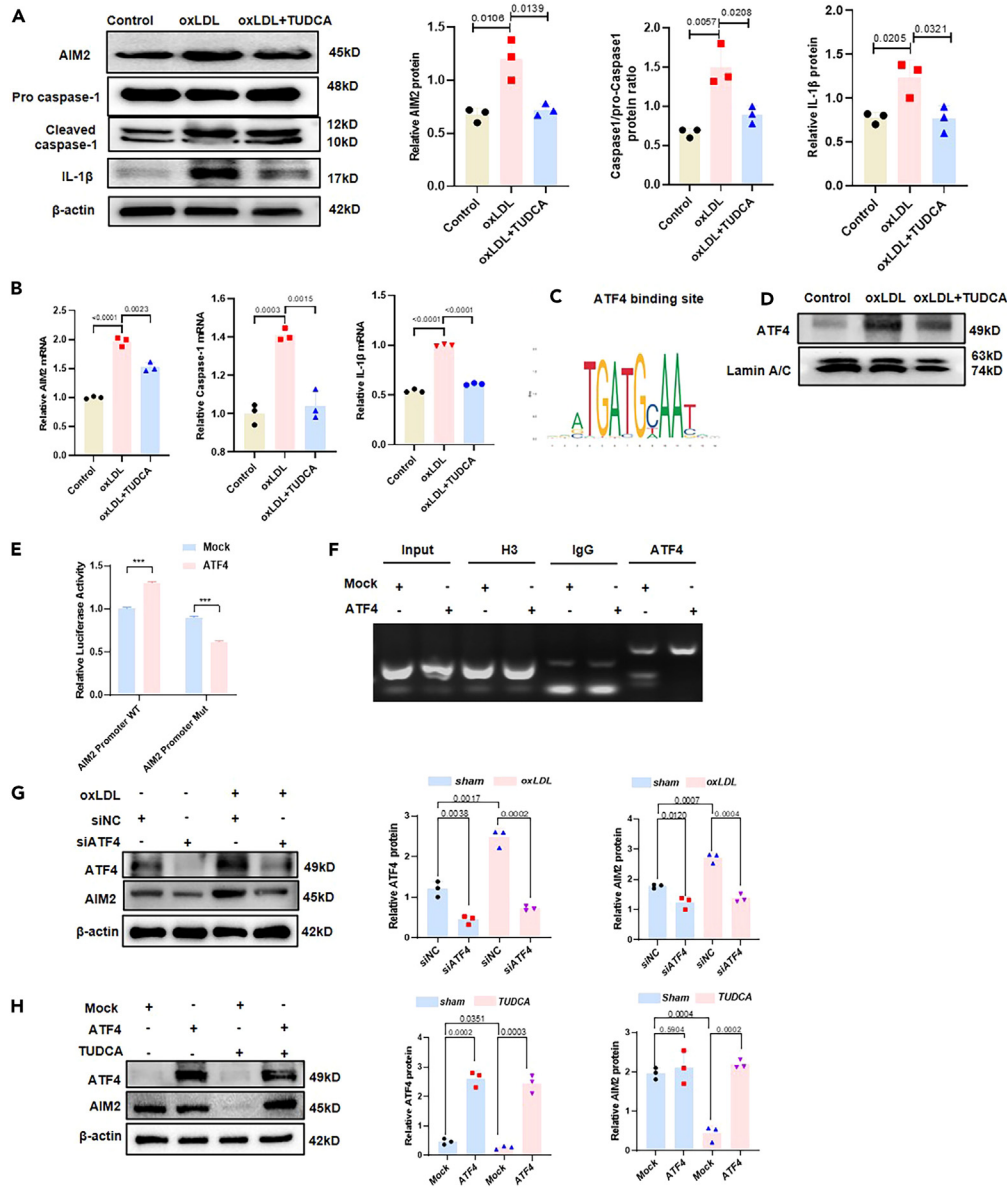
Figure 7. ATF4 binds to the AIM2 promoter to activate its transcription that is blocked by TUDCA

(A and B) RAW264.7 cells were stimulated with oxLDL after TUDCA pretreatment; the protein and mRNA expression of AIM2, caspase1, and IL-1β were detected by western blot and RT-qPCR (n = 3); t test. Data are represented as mean ± SD.

(C) Predicted bind site of the ATF4 to the AIM2 promoter by JASPAR database.

(D) THP-1 cells were stimulated with oxLDL after TUDCA pretreatment; nuclear ATF4 expression were detected by western blot (n = 3).

(E) THP-1 cells cotransfected with ATF4 expression plasmid or mock control, AIM2 wild-type (WT) or mutation (Mut) promoter-luciferase reporter plasmid and pRL-TK plasmid. Forty-eight hours after the transfection, the cells were subjected to luciferase activity analysis using a dual-luciferase reporter assay (n = 5); unpaired t test. Data are represented as mean ± SD.

(F) DNA agarose gel electrophoresis of ATF4 promoter DNA quantification using the ChIP assay with specific primer. Data are represented as mean +/SD.

(G) THP-1 cells were transfected with siATF4 for 8 h; the expression levels of ATF4 and AIM2 were detected by western blot (n = 3); t test. Data are represented as mean ± SD.

(H) THP-1 cells were transfected with ATF4 for 48 h; the expression levels of ATF4 and AIM2 were detected by western blot (n = 3); t test. Data are represented as mean ± SD.

RAW264.7 macrophage *in vitro*. The protein expression of AIM2, NLRP3, and IL-1β decreased as TUDCA concentration increased (Figure S4C). Furthermore, oxLDL increased the mRNA and protein expression of the AIM2/caspase-1/IL-1β axis, whereas TUDCA partly blocked the effect of oxLDL on macrophages in terms of AIM2 inflammasome activation (Figures 7A and 7B).

To further investigate the mechanism by which TUDCA inhibits AIM2 inflammasome activation, the matching ATF4-binding motif in the AIM2 promoter region was predicted and identified using the JASPAR database (Figure 7C). Also, TUDCA treatment reduced the nuclear ATF4 expression when stimulated with oxLDL (Figure 7D). We hypothesized that TUDCA decreased AIM2 transcription by inhibiting the transcription factor ATF4 expression, and ATF4 might bind to the promoter region of AIM2 and promote its mRNA expression. To validate this hypothesis, the wild-type and mutant AIM2 promoter plasmids were constructed and luciferase reporter assay was performed. We found that ATF4 overexpression increased the activity of the AIM2 luciferase reporter but did not increase the AIM2 luciferase reporter containing a mutation in the AIM2-binding site (Figure 7E). Also, chromatin immunoprecipitation assay confirmed that ATF4 binds to the AIM2 promoter in THP-1 cells (Figure 7F). Additionally, oxLDL stimulation promoted AIM2 expression, whereas ATF4 inhibition by siATF4 significantly blocked AIM2 expression (Figure 7G). Moreover, ATF4 overexpression enhanced AIM2 expression, whereas TUDCA treatment diminished it (Figure 7H). In conclusion, ATF4 binds to the AIM2 promoter and promotes AIM2 expression.

AIM2 inflammasome activation promotes the cholesterol storage by mediating ABCA1 expression

TUDCA alleviated the foam cell formation and increased the ABCA1 expression. And feature plot showed the gene expression of Abca1, Cd36, Il1b, and Gsdmd in the macrophage subpopulation in LDL$^{-/-}$ mice and human plaque tissues. Notably, macrophages with high IL-1β expression showed low ABCA1 expression in the macrophage subpopulation (Figure 8A). A previous study showed that NLRP3-mediated inflammasome activation inhibited cholesterol efflux, little is known about the role of AIM2 inflammasome. In our study, we found that ABCA1 protein expression increased and IL-1β/GSDMD-N expression decreased significantly after inhibiting AIM2 by AIM2 siRNA (Figure 8B). Immunofluorescence analysis showed that inhibition of AIM2 increased the expression of ABCA1 in the plasma membrane of macrophages (Figure 8C). In addition, Dil-LDL and oil-red staining showed that inhibition of AIM2 significantly alleviated the lipid storage of macrophage (Figure 8D). To further explore whether TUDCA inhibition of foam cell formation can be blocked by increasing AIM2 inflammasome activation, we transfected cells with the lvAIM2 before TUDCA treatment and found that AIM2 overexpression blocked the role of TUDCA in increasing ABCA1 in macrophages (Figure 8E).

DISCUSSION

Extensive evidence supports the theory that atherosclerosis is a chronic inflammatory process. Recently, increasing evidence has shown that cholesterol storage in macrophages is influenced by the inflammasome.[31] In this study, we established a link between dyslipidemia-induced ER stress, inflammasome activation, and cholesterol efflux in macrophages, as supported by the following: (1) scRNA-seq data showed an increased ER stress signal (as seen with expression of Eif2ak3, Eif2s1, Atf4) and increased inflammasome activation (as seen with expression of GSDMD, IL-18, and IL-1β) in macrophage cluster of the artery of LDL$^{-/-}$ mice fed the high-fat diet. Additionally, macrophage that expressed a high level of ATF4 also expressed higher levels of IL-1β and GSDMD than macrophages that expressed a low level of ATF4. (2) Treatment with TUDCA significantly alleviated plaque formation and resulted in a lower proportion of plaques with a necrotic core, decreased accumulation of macrophage, and increased the cholesterol efflux capacity of macrophage induced by the high-fat diet. TUDCA also decreased the activation of PERK/eIF2a/ATF4 axis and inflammasome. (3) TUDCA increased the expression of cholesterol transporter ABCA1, decreased AIM2-mediated inflammasome activation, and alleviated oxLDL-induced foam cell formation by macrophages in vitro. Further experiments demonstrated that TUDCA's protective role is partly through inhibition of the ER stress axis, PERK/eIF2a/ATF4. Normally, the transcription factor ATF4 binds to the AIM2 promoter, increases AIM2 transcription, and influences inflammasome activation, a process that TUDCA blocks. (4) Clusters with high IL-1β expression presented with low ABCA1 expression in the macrophage of artery plaques, whereas macrophages with high ABCA1 expression presented with low IL-1β levels, indicating a characteristic transformation from non-inflammatory-response-related macrophage with normal cholesterol efflux capacity to inflammatory macrophages with a damaged cholesterol efflux capacity. NLRP3-mediated inflammasome activation is known to influence ABCA1-mediated cholesterol storage, little was once known regarding how AIM2 influences the cholesterol efflux process. Our study showed that the AIM2 inflammasome participates in this process by regulating ABCA1 in macrophage during foam cell formation.

The Canakinumab Anti-Inflammatory Thrombosis Outcome Study (CANTOS) trial demonstrated that treatment with IL-1β monoclonal antibody (canakinumab) significantly reduced major adverse cardiovascular events and induced revascularization in patients with stable atherosclerosis.[32] However, canakinumab treatment has not been clinically authorized for the treatment of cardiovascular disease as it suppresses natural immune responses, leading to a minor risk of infection. Therefore, other drugs that target the inflammasomes are required. As described earlier, activation of AIM2 is an important process in transforming pro-IL-1β and plays a vital role in advanced atherosclerosis.[33] Compared with the activation mechanism of the NLRP3 inflammasome, AIM2 displayed different activation mechanisms, and recent studies have shown that AIM2 is linked to the atherosclerosis and Janus kinase 2 (JAK2)-mediated clonal hematopoiesis.[34–36] AIM2 might be an important target for precision medicine of atherosclerosis.[37] Therefore, this study provides a potential pharmacological intervention targeting the AIM2 inflammasome in atherosclerotic cardiovascular disease.

Previous studies have shown a loop reaction between cholesterol efflux and inflammasome activation. Myeloid ABCA1 deficiency has been shown to increase plasma IL-18 levels in Ldlr$^{-/-}$ mice and induce IL-1β and IL-18 secretion in splenocytes, which is reversed by NLRP3 or Caspase-1/11 deficiency.[19] Another study found that ABCA1 expression reduces membrane pore formation by inhibiting binding of GSDMD-N to the cell membrane and preventing cell lysis, which is attributed to ABCA1-induced phosphatidylinositol 4,5-bis-phosphate (PIP2) translocation.[38] Furthermore, inflammasome-mediated production of active IL-1β inhibits cholesterol efflux by targeting the expression of the ABCA1 and ABCG1, indicating a loop reaction between inflammasomes and membrane lipid transport proteins.[39] However, little is
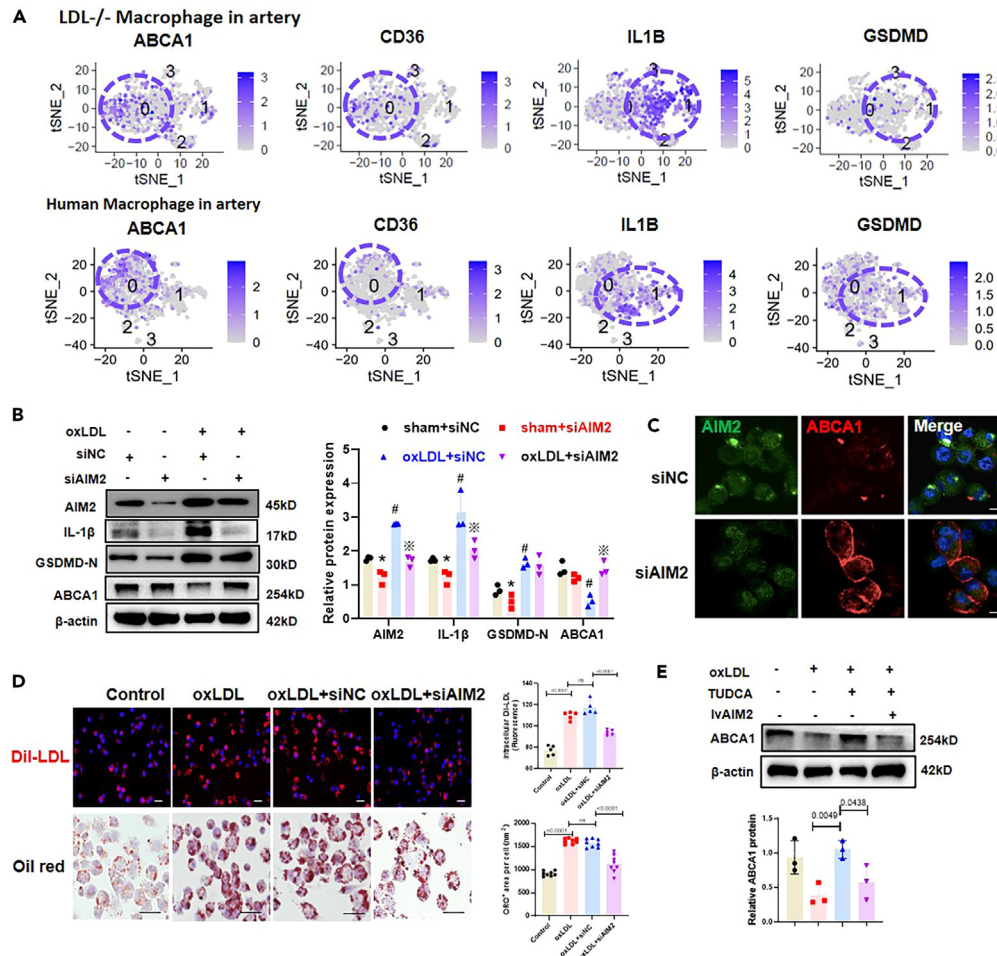
Figure 8. TUDCA alleviates lipid storage in macrophage by reducing AIM2 inflammasome activation and ABCA1-mediated cholesterol efflux

(A) t-SNE visualization of feature plot showed the gene expression of Abca1, Cd36, Il1b, and Gsdmd in the macrophage subpopulation in LDL$^{-/-}$ mice and human plaque tissues. The scale on the right of each gene indicates level of expression. Analysis was performed on published single-cell RNA sequencing data.

(B) RAW264.7 macrophages were transfected with siAIM2 for 8 h; the expression levels of AIM2, IL-1β, GSDMD-N, and ABCA1 were detected by western blot (n = 3) (*$p < 0.05$ between sham+siNC group and sham+siAIM2 group; #$p < 0.05$ between sham+siNC group and oxLDL+siNC group); t test. Data are represented as mean ± SD. ※$p < 0.05$ between oxLDL+siNC group and oxLDL+siAIM2 group.

(C) Immunofluorescence staining of AIM2 and ABCA1 after the RAW264.7 cells were transfected with siAIM2. Scale bars: 20 μm.

(D) RAW264.7 macrophages were transfected with siAIM2; lipid storage was calculated by Dil-LDL staining and oil red O staining. (n = 4); t test. Data are represented as mean ± SD. Scale bars = 10 μm.

(E) RAW264.7 macrophages were transfected with lvAIM2 for 48 h, then TUDCA was added. The expression levels of ABCA1 were detected by western blot (n = 3); t test. Data are represented as mean ± SD.

known regarding the relationship between the AIM2 inflammasome and ABCA1-/ABCG1-mediated cholesterol storage. It is shown that AIM2 inflammasome activation in macrophages drives necrotic core formation in atherosclerotic lesions. Notably, it has been demonstrated that JAK2 mutant macrophages suffered from the DNA replication stress and AIM2 inflammasome activation, thereby aggravating atherosclerosis.[36] Another study observed attenuated cholesterol efflux from macrophages of JAK2 mutant mice, most likely due to dysfunctional cholesterol transporter ABCA1, whereas cholesterol uptake was unaffected.[34,40,41] Our study provided the evidence that AIM2 inflammasome activation influences the ABCA1 expression, which may be a potential mechanism underlying the exacerbation of atherosclerosis during clonal hematopoiesis. Based on previously published results, there is a link between inflammasome activation and cholesterol efflux. It is shown that proinflammatory cytokine IL-1β triggers a negative feedback loop to inhibit ABCA1 expression and cholesterol efflux.[19,39,40] Also, GSDMD expression in macrophages exacerbated defects in reverse cholesterol transport and increased foam cell formation in an IL-1β-dependent fashion.[38] Our results showed that we hypothesize that this effect of AIM2 on the ABCA1 may be mediated by increasing the expression and activation of inflammasome-related proteins including IL-1β or GSDMD. Further studies on the IL-1β and GSDMD are required to clarify the potential mechanisms of AIM2 regulating the ABCA1 expression in macrophages.

Classically, it is theorized that foam cells in the necrotic core of plaque are mainly formed by circulating macrophage and monocyte recruited by dysfunctional ECs. Smooth muscle cells from the medium of blood vessels reportedly play an important role in the phenotypic modulation of macrophages and foam cell formation.[41] This phenotypic modulation of smooth muscle cells into macrophage-like cells in atherosclerosis is driven by ER stress as mediated by PERK and ATF4.[41,42] Our work supports these findings as we discovered that there is a high level of ATF4 expression in smooth muscle cells. Thus, further research is required to clarify the origin of ATF4-expressing foam cells, whether it is from circulating monocytes and macrophage or macrophage-like cells translated from the activated vascular smooth cells.

Bile acids exert multiple influences on inflammatory responses and regulate ER stress in various diseases.[43] As a conjugated bile acid derivative, TUDCA has been shown to rescue nonalcoholic fatty liver disease (NAFLD) by alleviating ER stress and inflammation, suppressing lipid transport and decreasing the intestinal inflammation level during dextran-sulfate-sodium-induced colitis in mice.[44,45] With respect to cardiovascular diseases, ER stress has been demonstrated to underly early heart failure caused by hypoplastic left heart syndrome, which can be rescued by TUDCA treatment.[46] In fact, TUDCA alleviates ER stress in multiple cardiovascular diseases, including neointimal hyperplasia, metabolic-syndrome-induced cardiovascular complications, and cardiorespiratory dysfunction.[47–49] In our study, we demonstrated the efficacy of TUDCA in alleviating atherosclerosis, and, consistent with a previous study,[44] reducing lipid droplets in hepatic tissues after an HFD. Therefore, our work demonstrates an additional protective role of TUDCA in treating the cluster of conditions characterized by metabolic syndrome, such as obesity, hypertension, insulin resistance, and dyslipidemia, which commonly cause multiple diseases, including atherosclerotic coronary artery disease, NAFLD, and diabetes. However, a limitation of our work is that we merely investigated the role of TUDCA in mice. Thus, further research in humans is required, and the safety and efficiency of TUDCA in preventing or treating atherosclerotic cardiovascular diseases in humans should be evaluated.

Conclusion

Taken together, this work adds to the growing knowledge surrounding macrophage transformation into foam cells in atherosclerosis by ER stress and inflammasome activation. This study extends our knowledge of the role of ATF4-mediated AIM2 inflammasome activation and provides a potential treatment strategy for targeting the PERK/eIF2a/ATF4 axis and inflammasome activation by ER stress alleviator TUDCA.

Limitations of the study

However, this work still has some limitations. Our work showed that ATF4 takes important role in regulating the AIM2 inflammasome activation after TUDCA treatment *in vitro*, whereas it still lacks relative evidences about whether overexpression of ATF4 can block the function of TUDCA on the reducing plaque and alleviate the cholesterol efflux capacity of macrophage in the atherosclerosis *in vivo*. Further studies are needed to support more experimental evidence on it.

STAR★METHODS

Detailed methods are provided in the online version of this paper and include the following:

- KEY RESOURCES TABLE
- RESOURCES AVAILABILITY
  - Lead contact
  - Materials availability
  - Date and code availability
- EXPERIMENTAL MODEL AND STUDY PARTICIPANT DETAILS
  - Patient samples
  - Mice
  - Cell lines
- METHOD DETAILS
  - scRNA sequencing analyses
  - Chromatin immunoprecipitation assay (ChIP)
  - Dual-luciferase reporter assay
  - Cholesterol efflux capacity
  - Atherosclerotic lesion analyses
  - Detection of plasma lipid
  - Immunohistochemistry
  - Immunofluorescence
  - Bulk-RNA sequencing and analyses
  - Cell culture and treatment
  - Oil Red O staining of cell
  - Dil-oxLDL uptake assay
  - Quantitative real time-PCR
  - Western blot

- QUANTIFICATION AND STATISTICAL ANALYSIS
  - Statistical analysis

SUPPLEMENTAL INFORMATION

ACKNOWLEDGMENTS

AUTHOR CONTRIBUTIONS

X.G. supervised the project, design, interpretation, manuscript revision, and final approval of the version to be submitted. X.W., Y.Z., and L.D. performed most of the experimental work; Z.J. and Y.G. performed *in vivo* animal experiments. K.W., Y.Z., and X.Y. helped with data analysis and manuscript revision. All authors reviewed and approved the final manuscript.

DECLARATION OF INTERESTS

The authors declare no conflicts of interests.

REFERENCES

1. Libby, P. (2021). The changing landscape of atherosclerosis. Nature *592*, 524–533.
2. Tsao, C.W., Aday, A.W., Almarzooq, Z.I., Alonso, A., Beaton, A.Z., Bittencourt, M.S., Boehme, A.K., Buxton, A.E., Carson, A.P., Commodore-Mensah, Y., et al. (2022). Heart Disease and Stroke Statistics-2022 Update: A Report From the American Heart Association. Circulation *145*, e153–e639.
3. Kobiyama, K., and Ley, K. (2018). Atherosclerosis. Circ. Res. *123*, 1118–1120.
4. Bäck, M., Yurdagul, A., Jr., Tabas, I., Oorni, K., and Kovanen, P.T. (2019). Inflammation and its resolution in atherosclerosis: mediators and therapeutic opportunities. Nat. Rev. Cardiol. *16*, 389–406.
5. In Het Panhuis, W., Schönke, M., Modder, M., Tom, H.E., Lalai, R.A., Pronk, A.C.M., Streefland, T.C.M., van Kerkhof, L.W.M., Dollé, M.E.T., Depuydt, M.A.C., et al. (2023). Time-restricted feeding attenuates hypercholesterolaemia and atherosclerosis development during circadian disturbance in APOE*3-Leiden.CETP mice. EBioMedicine *93*, 104680.
6. Tabas, I., and Bornfeldt, K.E. (2016). Macrophage Phenotype and Function in Different Stages of Atherosclerosis. Circ. Res. *118*, 653–667.
7. Cochain, C., and Zernecke, A. (2017). Macrophages in vascular inflammation and atherosclerosis. Pflügers Archiv *469*, 485–499.
8. Libby, P., Ridker, P.M., and Hansson, G.K. (2011). Progress and challenges in translating the biology of atherosclerosis. Nature *473*, 317–325.
9. Baumer, Y., Mehta, N.N., Dey, A.K., Powell-Wiley, T.M., and Boisvert, W.A. (2020). Cholesterol crystals and atherosclerosis. Eur. Heart J. *41*, 2236–2239.
10. Yvan-Charvet, L., Wang, N., and Tall, A.R. (2010). Role of HDL, ABCA1, and ABCG1 transporters in cholesterol efflux and immune responses. Arterioscler. Thromb. Vasc. Biol. *30*, 139–143.
11. Cochain, C., Vafadarnejad, E., Arampatzi, P., Pelisek, J., Winkels, H., Ley, K., Wolf, D., Saliba, A.E., and Zernecke, A. (2018). Single-Cell RNA-Seq Reveals the Transcriptional Landscape and Heterogeneity of Aortic Macrophages in Murine Atherosclerosis. Circ. Res. *122*, 1661–1674.
12. Colin, S., Chinetti-Gbaguidi, G., and Staels, B. (2014). Macrophage phenotypes in atherosclerosis. Immunol. Rev. *262*, 153–166.
13. Tong, W., Zhang, Y., Hui, H., Feng, X., Ning, B., Yu, T., Wang, W., Shang, Y., Zhang, G., Zhang, S., et al. (2023). Sensitive magnetic particle imaging of haemoglobin degradation for the detection and monitoring of intraplaque haemorrhage in atherosclerosis. EBioMedicine *90*, 104509.
14. Gisterå, A., and Hansson, G.K. (2017). The immunology of atherosclerosis. Nat. Rev. Nephrol. *13*, 368–380.
15. Bakhshi, H., Michelhaugh, S.A., Bruce, S.A., Seliger, S.L., Qian, X., Ambale Venkatesh, B., Varadarajan, V., Bagchi, P., Lima, J.A.C., and deFilippi, C. (2023). Association between proteomic biomarkers and myocardial fibrosis measured by MRI: the multi-ethnic study of atherosclerosis. EBioMedicine *90*, 104490.
16. Núñez, E., Fuster, V., Gómez-Serrano, M., Valdivielso, J.M., Fernández-Alvira, J.M., Martínez-López, D., Rodríguez, J.M., Bonzon-Kulichenko, E., Calvo, E., Alfayate, A., et al. (2022). Unbiased plasma proteomics discovery of biomarkers for improved detection of subclinical atherosclerosis. EBioMedicine *76*, 103874.
17. Du, L., Wang, X., Chen, S., and Guo, X. (2022). The AIM2 Inflammasome: A Novel Biomarker and Target in Cardiovascular Disease. Pharmacol. Res. *186*, 106533.
18. Martínez, G.J., Celermajer, D.S., and Patel, S. (2018). The NLRP3 inflammasome and the emerging role of colchicine to inhibit atherosclerosis-associated inflammation. Atherosclerosis *269*, 262–271.
19. Westerterp, M., Fotakis, P., Ouimet, M., Bochem, A.E., Zhang, H., Molusky, M.M., Wang, W., Abramowicz, S., la Bastide-van Gemert, S., Wang, N., et al. (2018). Cholesterol Efflux Pathways Suppress Inflammasome Activation, NETosis, and Atherogenesis. Circulation *138*, 898–912.
20. Westerterp, M., Gautier, E.L., Ganda, A., Molusky, M.M., Wang, W., Fotakis, P., Wang, N., Randolph, G.J., D'Agati, V.D., Yvan-Charvet, L., and Tall, A.R. (2017). Cholesterol Accumulation in Dendritic Cells Links the Inflammasome to Acquired Immunity. Cell Metabol. *25*, 1294–1304.e6.
21. Wu, M., Yang, Z., Zhang, C., Shi, Y., Han, W., Song, S., Mu, L., Du, C., and Shi, Y. (2021). Inhibition of NLRP3 inflammasome ameliorates podocyte damage by suppressing lipid accumulation in diabetic nephropathy. Metabolism *118*, 154748.
22. Dang, E.V., McDonald, J.G., Russell, D.W., and Cyster, J.G. (2017). Oxysterol Restraint of Cholesterol Synthesis Prevents AIM2 Inflammasome Activation. Cell *171*, 1057–1071.e11.
23. Ren, J., Bi, Y., Sowers, J.R., Hetz, C., and Zhang, Y. (2021). Endoplasmic reticulum stress and unfolded protein response in cardiovascular diseases. Nat. Rev. Cardiol. *18*, 499–521.
24. Marciniak, S.J., Chambers, J.E., and Ron, D. (2022). Pharmacological targeting of

endoplasmic reticulum stress in disease. Nat. Rev. Drug Discov. *21*, 115–140.

25. Hetz, C., Zhang, K., and Kaufman, R.J. (2020). Mechanisms, regulation and functions of the unfolded protein response. Nat. Rev. Mol. Cell Biol. *21*, 421–438.

26. Kim, S., Lee, S.E., Yi, S., Jun, S., Yi, Y.S., Nagar, H., Kim, C.S., Shin, C., Yeo, M.K., Kang, Y.E., and Oh, S.H. (2021). Tauroursodeoxycholic Acid Decreases Keloid Formation by Reducing Endoplasmic Reticulum Stress as Implicated in the Pathogenesis of Keloid. Int. J. Mol. Sci. *22*, 10765.

27. Rani, S., Sreenivasaiah, P.K., Kim, J.O., Lee, M.Y., Kang, W.S., Kim, Y.S., Ahn, Y., Park, W.J., Cho, C., and Kim, D.H. (2017). Tauroursodeoxycholic acid (TUDCA) attenuates pressure overload-induced cardiac remodeling by reducing endoplasmic reticulum stress. PLoS One *12*, e0176071.

28. Pan, H., Xue, C., Auerbach, B.J., Fan, J., Bashore, A.C., Cui, J., Yang, D.Y., Trignano, S.B., Liu, W., Shi, J., et al. (2020). Single-Cell Genomics Reveals a Novel Cell State During Smooth Muscle Cell Phenotypic Switching and Potential Therapeutic Targets for Atherosclerosis in Mouse and Human. Circulation *142*, 2060–2075.

29. Martini, E., Kunderfranco, P., Peano, C., Carullo, P., Cremonesi, M., Schorn, T., Carriero, R., Termanini, A., Colombo, F.S., Jachetti, E., et al. (2019). Single-Cell Sequencing of Mouse Heart Immune Infiltrate in Pressure Overload-Driven Heart Failure Reveals Extent of Immune Activation. Circulation *140*, 2089–2107.

30. Rutkowski, D.T., and Kaufman, R.J. (2003). All roads lead to ATF4. Dev. Cell *4*, 442–444.

31. Yvan-Charvet, L., Bonacina, F., Guinamard, R.R., and Norata, G.D. (2019). Immunometabolic function of cholesterol in cardiovascular disease and beyond. Cardiovasc. Res. *115*, 1393–1407.

32. Ridker, P.M., Everett, B.M., Thuren, T., MacFadyen, J.G., Chang, W.H., Ballantyne, C., Fonseca, F., Nicolau, J., Koenig, W., Anker, S.D., et al. (2017). Antiinflammatory Therapy with Canakinumab for Atherosclerotic Disease. N. Engl. J. Med. *377*, 1119–1131.

33. Paulin, N., Viola, J.R., Maas, S.L., de Jong, R., Fernandes-Alnemri, T., Weber, C., Drechsler, M., Döring, Y., and Soehnlein, O. (2018). Double-Strand DNA Sensing Aim2 Inflammasome Regulates Atherosclerotic Plaque Vulnerability. Circulation *138*, 321–323.

34. Du, L., Wang, X., Chen, S., and Guo, X. (2022). The AIM2 inflammasome: A novel biomarker and target in cardiovascular disease. Pharmacol. Res. *186*, 106533.

35. Bird, L. (2021). Taking AIM2 at atherosclerotic plaques. Nat. Rev. Immunol. *21*, 273.

36. Fidler, T.P., Xue, C., Yalcinkaya, M., Hardaway, B., Abramowicz, S., Xiao, T., Liu, W., Thomas, D.G., Hajebrahimi, M.A., Pircher, J., et al. (2021). The AIM2 inflammasome exacerbates atherosclerosis in clonal haematopoiesis. Nature *592*, 296–301.

37. Soehnlein, O., and Tall, A.R. (2022). AIMing 2 treat atherosclerosis. Nat. Rev. Cardiol. *19*, 567–568.

38. Opoku, E., Traughber, C.A., Zhang, D., Iacano, A.J., Khan, M., Han, J., Smith, J.D., and Gulshan, K. (2021). Gasdermin D Mediates Inflammation-Induced Defects in Reverse Cholesterol Transport and Promotes Atherosclerosis. Front. Cell Dev. Biol. *9*, 715211.

39. Tumurkhuu, G., Dagvadorj, J., Porritt, R.A., Crother, T.R., Shimada, K., Tarling, E.J., Erbay, E., Arditi, M., and Chen, S. (2018). Chlamydia pneumoniae Hijacks a Host Autoregulatory IL-1β Loop to Drive Foam Cell Formation and Accelerate Atherosclerosis. Cell Metabol. *28*, 432–448.e4.

40. Kim, M.Y., Ilyosbek, S., Lee, B.H., Yi, K.Y., and Jung, Y.S. (2017). A novel urotensin II receptor antagonist, KR-36676, prevents ABCA1 repression via ERK/IL-1β pathway. Eur. J. Pharmacol. *803*, 174–178.

41. Chattopadhyay, A., Kwartler, C.S., Kaw, K., Li, Y., Kaw, A., Chen, J., LeMaire, S.A., Shen, Y.H., and Milewicz, D.M. (2021). Cholesterol-Induced Phenotypic Modulation of Smooth Muscle Cells to Macrophage/Fibroblast-like Cells Is Driven by an Unfolded Protein Response. Arterioscler. Thromb. Vasc. Biol. *41*, 302–316.

42. Chattopadhyay, A., Guan, P., Majumder, S., Kaw, K., Zhou, Z., Zhang, C., Prakash, S.K., Kaw, A., Buja, L.M., Kwartler, C.S., and Milewicz, D.M. (2022). Preventing Cholesterol-Induced Perk (Protein Kinase RNA-Like Endoplasmic Reticulum Kinase) Signaling in Smooth Muscle Cells Blocks Atherosclerotic Plaque Formation. Arterioscler. Thromb. Vasc. Biol. *42*, 1005–1022.

43. Kusaczuk, M. (2019). Tauroursodeoxycholate-Bile Acid with Chaperoning Activity: Molecular and Cellular Effects and Therapeutic Perspectives. Cells *8*, 1471.

44. Latif, M.U., Schmidt, G.E., Mercan, S., Rahman, R., Gibhardt, C.S., Stejerean-Todoran, I., Reutlinger, K., Hessmann, E., Singh, S.K., Moeed, A., et al. (2022). NFATc1 signaling drives chronic ER stress responses to promote NAFLD progression. Gut *71*, 2561–2573.

45. Cao, S.S., Zimmermann, E.M., Chuang, B.M., Song, B., Nwokoye, A., Wilkinson, J.E., Eaton, K.A., and Kaufman, R.J. (2013). The unfolded protein response and chemical chaperones reduce protein misfolding and colitis in mice. Gastroenterology *144*, 989–1000.e6.

46. Xu, X., Jin, K., Bais, A.S., Zhu, W., Yagi, H., Feinstein, T.N., Nguyen, P.K., Criscione, J.D., Liu, X., Beutner, G., et al. (2022). Uncompensated mitochondrial oxidative stress underlies heart failure in an iPSC-derived model of congenital heart disease. Cell Stem Cell *29*, 840–855.e7.

47. Radwan, E., Bakr, M.H., Taha, S., Sayed, S.A., Farrag, A.A., and Ali, M. (2020). Inhibition of endoplasmic reticulum stress ameliorates cardiovascular injury in a rat model of metabolic syndrome. J. Mol. Cell. Cardiol. *143*, 15–25.

48. Kim, S.Y., Kwon, Y.W., Jung, I.L., Sung, J.H., and Park, S.G. (2011). Tauroursodeoxycholate (TUDCA) inhibits neointimal hyperplasia by suppression of ERK via PKCα-mediated MKP-1 induction. Cardiovasc. Res. *92*, 307–316.

49. Díaz, H.S., Andrade, D.C., Toledo, C., Schwarz, K.G., Pereyra, K.V., Díaz-Jara, E., Marcus, N.J., and Del Rio, R. (2021). Inhibition of Brainstem Endoplasmic Reticulum Stress Rescues Cardiorespiratory Dysfunction in High Output Heart Failure. Hypertension *77*, 718–728.

STAR★METHODS

KEY RESOURCES TABLE

REAGENT or RESOURCE	SOURCE	IDENTIFIER
Antibodies		
ABCA1	Abcam	Cat# ab7360; RRID:AB_305880
ABCG1	Abcam	Cat# ab52617; RRID:AB_867471
SR-B1	Abcam	Cat# ab217318; RRID:AB_303482
AIM2	CST	Cat# 63660; RRID:AB_2890193
NLRP3	CST	Cat# 15101; RRID:AB_2722591
IL-1β	CST	Cat# 31202; RRID:AB_2799001
Cleaved-IL-1β	CST	Cat# 63124; RRID:AB_2799639
Cleaved-GSDMD	CST	Cat# 34667; RRID:AB_2923068
Anti-proCaspase-1+p10+p12	Abcam	Cat# ab179515; RRID:AB_2884954
ATF4	Proteintech	Cat# 10835-1-AP; RRID:AB_2058600
PERK	CST	Cat# 4370; RRID:AB_2315112
ERK	CST	Cat# 4695; RRID:AB_390779
eIF2a	Abcam	Cat# ab169528; RRID:AB_2819002
Phospho-eIF2α(Ser51)	CST	Cat# 3398; RRID:AB_2096481
Moma-2	Abcam	Cat# ab33451; RRID:AB_776518
aSMA	Abcam	Cat# ab179467; RRID:AB_2737344
CD68	Abcam	Cat# ab53444(Mice) and ab289671(Human); RRID:AB_869007, AB_2801637
SM22(TAGLN)	Abcam	Cat# ab10135; RRID:AB_2255631
Biological samples		
Human healthy artery samples	First Affiliated Hospital of Zhejiang University School of Medicine (China)	N/A
Diseased carotid plaque samples	First Affiliated Hospital of Zhejiang University School of Medicine (China)	N/A
Chemicals, peptides, and recombinant proteins		
TUDCA	MCE	Cat# 14605-22-2
fetal bovine serum	Gibco	Cat# 10099141
ac-LDL	yiyuan	Cat# YB-004
Dil-ox-LDL	yiyuan	Cat# YB-0010
oxLDL	yiyuan	Cat# YB-002
Triton X-10	Sigma	Cat# 9002-93-01
4% PFA	Beyotime	Cat# 30525-89-4
TUDCA	MCE	Cat# 14605-22-2
Critical commercial assays		
SimpleChIP® Plus Enzymatic Chromatin IP Kit (Magnetic Beads)	Cell Signaling Technology	Cat# 9005
Dual-Luciferase Reporter Assay System	Promega	Cat# E1910
mouse TC elisa kit	jiancheng	Cat# A111-1-1
mouse LDL-C elisa kit	jiancheng	Cat# A113-1-1
mouse HDL-C elisa kit	jiancheng	Cat# A-112-1-1

Continued

REAGENT or RESOURCE	SOURCE	IDENTIFIER
mouse TG elisa kit	jiancheng	Cat# A-110-1-1
Enhanced BCA Protein Assay Kit	Beyotime	Cat# P0012
DAB Horseradish Peroxidase Color Development Kit	ZSGB-bio	Cat# ZLI-9017
Deposited data		
raw and analyzed Bulk-sequence data	Gene Expression Omnibus	GSE260610
public data: single cell RNA sequence	Gene Expression Omnibus	GEO:(GSE97310; GSE155514)
public data: microarray	Gene Expression Omnibus	GEO:(GSE43292)
Experimental models: Cell lines		
THP-1	ATCC	Cat# XY-XB-1266; RRID:CVCL_0006
RAW264.7	ATCC	Cat# BH0371; RRID:CVCL_C6X2
Experimental models: Organisms/strains		
Mouse:C57BL/6J wild type	HFK Bioscience Company	N/A
Mouse:C57BL/6J APOE-/-	HFK Bioscience Company	N/A
Oligonucleotides		
Primer: ABCA1_F GGAGCCTTTGTGGAACTCTTCC	TsingkeBiotechnology	https://tsingke.com.cn/
Primer: ABCA1_R CGCTCTCTTCAGCCACTTTGAG	TsingkeBiotechnology	https://tsingke.com.cn/
Primer: ABCG1_F GACACCGATGTGAACCCGTTTC	TsingkeBiotechnology	https://tsingke.com.cn/
Primer: ABCG1_R GCATGATGCTGAGGAAGGTCCT	TsingkeBiotechnology	https://tsingke.com.cn/
Primer: CD36_F GGACATTGAGATTCTTTTCCTCTG	TsingkeBiotechnology	https://tsingke.com.cn/
Primer: CD36_R GCAAAGGCATTGGCTGGAAGAAC	TsingkeBiotechnology	https://tsingke.com.cn/
Primer: AIM2_F AGGCTGCTACAGAAGTCTGTCC	TsingkeBiotechnology	https://tsingke.com.cn/
Primer: AIM2_R TCAGCACCGTGACAACAAGTGG	TsingkeBiotechnology	https://tsingke.com.cn/
Primer: NLRP3_F TCACAACTCGCCCAAGGAGGAA	TsingkeBiotechnology	https://tsingke.com.cn/
Primer: NLRP3_R AAGAGACCACGGCAGAAGCTAG	TsingkeBiotechnology	https://tsingke.com.cn/
Primer: IL1β_F TGGACCTTCCAGGATGAGGACA	TsingkeBiotechnology	https://tsingke.com.cn/
Primer: IL1β_R GTTCATCTCGGAGCCTGTAGTG	TsingkeBiotechnology	https://tsingke.com.cn/
Primer: ATF4_F AACCTCATGGGTTCTCCAGCGA	TsingkeBiotechnology	https://tsingke.com.cn/
Primer: ATF4_R CTCCAACATCCAATCTGTCCCG	TsingkeBiotechnology	https://tsingke.com.cn/
Primer: ATF6_F GTCCAAAGCGAAGAGCTGTCTG	TsingkeBiotechnology	https://tsingke.com.cn/
Primer: ATF6_R AGAGATGCCTCCTCTGATTGGC	TsingkeBiotechnology	https://tsingke.com.cn/

Continued

REAGENT or RESOURCE	SOURCE	IDENTIFIER
Primer: NFKB_F GCTGCCAAAGAAGGACACGACA	TsingkeBiotechnology	https://tsingke.com.cn/
Primer: NFKB_R GGCAGGCTATTGCTCATCACAG	TsingkeBiotechnology	https://tsingke.com.cn/
Primer: Gapdh_F TGTCGTGGAGTCTACTGGTG	TsingkeBiotechnology	https://tsingke.com.cn/
Primer: Gapdh_R ACACCCATCACAAACATGG	TsingkeBiotechnology	https://tsingke.com.cn/
Recombinant DNA		
h-AIM2-promoter-wt-ZV702	this paper	N/A
h-AIM2-promoter-mut-ZV702	this paper	N/A
Software and algorithms		
GraphPad Prism 8.0	GraphPad software	https://www.graphpad.com/
Image J	NIH	https://imagej.net/ij/
R 4.3.1	R project	https://www.r-project.org

RESOURCES AVAILABILITY

Lead contact

Further information and requests for resources and reagents should be directed to and will be fulfilled by the corresponding author, Prof. Dr. Xiaogang Guo (gxg22222@zju.edu.cn).

Materials availability

This study did not generate new unique reagents.

Date and code availability

- Raw data and processed data of RNA-seq datasets generated during this study have been deposited on GEO(GSE260610) and are publicly available as of the date of publication.
- This paper does not report original code.
- Any additional information required to reanalyze the data reported in this paper is available from the lead contact upon request.

EXPERIMENTAL MODEL AND STUDY PARTICIPANT DETAILS

Patient samples

Human healthy artery samples were collected from the branches of the aorta of the receptor in patients who underwent lung transplant surgeries. Diseased carotid plaque specimens were collected from patients who were diagnosed with carotid stenosis and underwent the carotid endarterectomy (CEA) at the First Affiliated Hospital of Zhejiang University School of Medicine (China) between June 2015 and December 2020. Exclusion criteria for enrolment were established ahead of time, including the presence of major organ diseases such as liver failure, dialysis, cancer, chemotherapy, and pregnancy, as well as lack of consent to participate in the study. Patients' characteristics were summarized in the Table S1. Informed consent was obtained from all patients, which clearly stated the purpose of our study. Study protocol was approved by the Research Ethics Committees of the First Affiliated Hospital of Zhejiang University (Institutional Review Board approval No. 2021/330), and written informed consent was obtained from all patients, which clearly stated the purpose of our study.

Mice

All mice studies were sanctioned by the Animal Ethics Committee of Zhejiang University; the care and use of animals followed the guidelines on animal ethics (Institutional Review Board approval No. 2021/330). Male ApoE$^{-/-}$ mice (8 weeks old, n =60) were obtained from HFK Bioscience Company (Beijing, China). All the ApoE$^{-/-}$ mice were randomly divided into 3 groups (n = 20 per group): Group 1: control group (normal fat diet, NFD); Group 2: high-fat diet (HFD); Group 3: HFD + TUDCA. A random number table was used for mouse randomization. Group 1 mice were fed with a diet of 5% fat without cholesterol, whereas the other groups were fed with an HFD (16% fat and 0·25% cholesterol). All mice were provided with food and water and subjected to a light-dark cycle in an environment at 20°C-22°C and 50%-60% humidity. After 8 weeks of HFD feeding, one group of HFD-treated mice was intragastric administration with 1000 mg/kg of TUDCA once daily (HFD+TUDCA

group) for 4 weeks, whereas the NFD-treated mice and other group of HFD-treated mice were treated with an equal volume of saline (NFD or HFD group) for 4 weeks. After 4 weeks of TUDCA or saline treatment, the mice were anaesthetized intraperitoneally with 3% pentobarbital sodium (40 mg/kg) and sacrificed. The aortic tissues from the ascending aorta to the ileal bifurcation and hearts were immediately gathered for histological staining, western blotting (WB), bulk-RNA sequencing or Oil Red O staining, and the serum samples were collected for subsequent experiments.

Cell lines

Macrophages (THP-1 cell lines (Cat# XY-XB-1266) and RAW264.7 cell lines (Cat# BH0371)) purchased from ATCC (USA) were cultured in the Dulbecco's modified eagle medium (DMEM glucose 5.5 mM) supplemented with 10% fetal bovine serum (FBS) in an atmosphere at 37°C and 5% CO2. The cell lines have been authenticated through PCR with pairs of Short Tandem Repeat (STR). All the experiments were conducted using mycoplasma-free cells, and mycoplasma contamination has been monitored using PCR methods.

METHOD DETAILS

scRNA sequencing analyses

The data and R scripts that related to the findings of this study are available on reasonable request. ScRNA-seq data of this study are available in Gene Expression Omnibus[11,28] (GSE97310; GSE155514). Analysis of processed scRNA-seq data were carried out in R version 4.0 using the Seurat suite versions3.2.3. R scripts containing the steps used for processing and clustering the data for each individual data-set. For all datasets, initial quality control filtering metrics were applied as follows: Low quality cells (<400 genes/ cell, >20000 genes/ cell and >10 % mitochondrial transcript presence/ cell) were excluded from downstream analysis. To remove the batch effect, the datasets collected from different samples were integrated using Seurat v3 with default parameters.

Data were then log-normalized for subsequent analysis. Dimensionality reduction using PCA was undertaken to explore transcriptional heterogeneity and perform cell clustering. 30 PCs were selected that explained more variability than expected by chance using heuristics detailed in vignettes associated with the Seurat software. PC loadings were used as input for a graph-based approach to cluster cells by cell type, and as input for UMAP for reduction to two dimensions for visualization purposes. Markers for a specific cluster against all remaining cells were found with function FindAllMarkers (Arguments: only.pos=TRUE, min.pct=0.25, logfc.threshold = 0.25). Gene ontology (GO) and Kyoto encyclopedia of genes and genomes pathway analysis were performed with marker genes of each cluster found by FindAllMarkers function or enriched genes found by FindMarkers function with average log (fold change) >0.25 on Metascape website (the database for annotation, visualization and integrated discovery).

Chromatin immunoprecipitation assay (ChIP)

Chromatins extracted from transfected THP-1 cells were fixed and then immunoprecipitated using the commercial kit (9005, Cell Signaling Technology) according to the manufacturer's instructions. The purified chromatins were immunoprecipitated using 2μg of anti-HA. The binding between ATF4(NM_182810) and *AIM2* promoter was assessed by PCR. The average size of the sonicated DNA fragments subjected to immunoprecipitation was 230bp as determined by ethidium bromide gel electrophoresis. The *AIM2* primers for ChIP as followed: forward 5'-TAGCTCACCCTAGTCCCACC-3' and reverse 5'-TTCCAAGGGCTTCTCATGCT-3'.

Dual-luciferase reporter assay

We first constructed the wild type and mutant AIM2 promoter plasmids (h-AIM2-promoter-wt-ZV702 or h-AIM2-promoter-mut-ZV702) by referring to the binding site between ATF4 and AIM2 promoter region. 293T cells were seeded overnight in 12-well plates and then co-transfected with firefly luciferase plasmid (0.5 μg) expressing the wild-type *AIM2* promoter, or *AIM2* mutation promoter (0.5 μg) and Renilla luciferase expressing plasmid (0.01 μg, Vigene Biology, Jinan, China). About 48h after transfection, cells were harvested to determine the luciferase activity using a Dual-Luciferase Reporter Assay System (E1910, Promega), following the manufacturer's instructions. The firefly luciferase data were normalized to the Renilla luciferase data, which were expressed as the fold change relative to the control. The dual-luciferase reporter assay was conducted with six replicates in each group. The test was performed at least in triplicate.

Cholesterol efflux capacity

For isolation of peritoneal macrophage, Apoe-/- mice were placed in an anesthesia induction box connected to the vaporizer with 3.0 Vol% isoflurane and a 100% oxygen flow of 1 L/min to induce global anesthesia. The peritoneal cavity was exposed by making a small incision in the abdominal skin and muscle layers, careful to avoid damaging internal organs. Phosphate-buffered saline (PBS, pH 7.4) containing 3% fetal bovine serum (FBS) was then injected into the peritoneal cavity using a syringe equipped with a 25-gauge needle. The volume of PBS used varied according to the mouse's size, typically between 5 to 10 mL. After gentle massage of the abdomen for 2-3 minutes to facilitate the detachment of macrophages from the peritoneal lining, the peritoneal fluid was aspirated using the same syringe. The macrophages were embedded with Dulbecco's Modified Eagle Medium (DMEM, Gibco) with 10uCi/ml [3 H]-cholesterol plus 100 μg/mL ac-LDL for 48 h and then suspended in DMEM. Subsequently, macrophages labeled with [3 H]-cholesterol (5×106 cells/mouse) were intraperitoneally injected into three group mice (n=5 in each group). Plasma samples and hepatic tissue specimens were obtained at 72h after injection. The feces were

continuously collected until 72h. The radioactivity of [3 H]-cholesterol in the plasma, liver and feces were analyzed by a liquid scintillation counter and showed as the H value.

Atherosclerotic lesion analyses

Aortic tissues from the mice ascending aorta to the ileal bifurcation were fixed in 4% paraformaldehyde solution and the adventitia was thoroughly cleaned under the dissecting microscope (n = 5 per group). The aortas were incised longitudinally and stained with Oil Red O(ORO) for 30 min and then photographed using a digital camera. The hearts with attached aortic roots were embedded in OCT and sectioned at 6μm. Slides were stained with ORO, masson and hematoxylin eosin staining following the manufacturer's protocol. The atherosclerotic lesions in the aorta were quantified by *en face* analysis and aortic root cross-sectional measurement. Measurement of the aortic atherosclerotic lesions was performed blind to the group of mice.

Detection of plasma lipid

Blood samples were collected from the retro-orbital plexus of mice at the end of experiments and then centrifuged at 1000 g for 15 min to isolate the plasma. The levels of total cholesterol (TC), low density lipoprotein cholesterol (LDL-C), HDL cholesterol (HDL-C) and total triglyceride (TG) in plasma were measured by using the available enzymatic kits (Jiancheng, Nanjing, China).

Immunohistochemistry

Tissue sections were deparaffinized and hydrated in gradient xylene and ethanol. Sections were then incubated in 3% H_2O_2 for 10 mins to quench endogenous peroxidase activity. Antigen retrieval was performed by 98°C water bath for 25 mins. Antigen retrieval solution used was prepared as 10mM Tris, 1 mM EDTA and 0.05% Tween-20 (pH 9.0). After cooling down to room temperature (RT), tissue was blocked and permeabilized with 5% BSA+0.1% Triton X-100 (Sigma, T8787) for 1 hour at RT, and stained with primary antibodies overnight, then incubated with HRP conjugated secondary antibodies for 1 h at 37°C. Sections were then incubated in horseradish peroxidase substrate solution (3,3NDiaminobenzidine Tertrahydrochloride, DAB Horseradish Peroxidase Color Development Kit, ZSGB-bio, ZLI-9017, 1:20). The time for color development was carefully observed under a microscope. After coloration, sections were counterstained with hematoxylin for 5 mins, then dehydrated through increasing concentrations of ethanol and xylene, and finally mounted with neutral resin. A PANNORAMIC 250 Flash slide scanner (3DHISTECH) was used to acquire images. The Image pro plus 6.0 software (Media Cybernetics, Inc.) was used for image analyses. For each section, the whole field of view of an artery was captured. The investigators were blinded to different groups when performing immunostaining and analyzing the data.

Immunofluorescence

For immunofluorescence staining of cryo-sections from mouse samples, aortic sinus was first harvested, washed with PBS and fixed in 4% paraformaldehyde at 4°C for 2 h, followed by dehydration in 30% sucrose solution at 4°C overnight until fully penetrated. Tissues were then embedded in optimum cutting temperature (O.C.T., Sakura, 4583), frozen at -80°C for storage, or cut into 5-μm sections by a Cryostat (Leica CM1950). Cryosections were air-dried for about 30 mins at room temperature, blocked and permeabilized in 5% donkey serum (with 0.1% Triton X-100 in PBS) for 1 h, stained with primary antibodies overnight at 4°C, then incubated with Alexa Fluor-conjugated secondary antibodies (Invitrogen, 1:500) for 1 h, followed by DAPI staining and mounting in the anti-fade mounting medium. A Nikon A1 Ti confocal microscope was used to acquire cryo-section, en-face and cell staining images, further analyzed by relevant software. Regions were selected randomly to avoid biasing. For quantification of immunostaining images, at least 3 random fields of view containing the whole artery were counted and the mean values were taken as the data point for each mouse sample. The investigators were blinded to different groups when performing immunostaining and analyzing the data.

Bulk-RNA sequencing and analyses

Total RNA was extracted using Trizol reagent kit (Invitrogen, Carlsbad, CA, USA) according to the manufacturer's protocol. RNA quality was assessed on an Agilent 2100 Bioanalyzer (Agilent Technologies, Palo Alto, CA, USA) and checked using RNase free agarose gel electrophoresis. After total RNA was extracted, eukaryotic mRNA was enriched by Oligo(dT) beads. Then the enriched mRNA was fragmented into short fragments using fragmentation buffer and reversly transcribed into cDNA by using NEBNext Ultra RNA Library Prep Kit for Illumina (NEB #7530,New England Biolabs, Ipswich, MA, USA).The purified double-stranded cDNA fragments were end repaired, A base added, and ligated to Illumina sequencing adapters. The ligation reaction was purified with the AMPure XP Beads (1.0X). Ligated fragments were subjected to size selection by agarose gel electrophoresis and polymerase chain reaction (PCR) amplified. The resulting cDNA library was sequenced using Illumina Novaseq6000 by Gene Denovo Biotechnology Co. (Guangzhou, China). Principal component analysis (PCA) was performed with R package gmodels in this experiment. RNAs differential expression analysis were performed by DESeq2 software between two groups. The genes/transcripts with parameter of false discovery rate (FDR) below 0.05 and absolute fold change≥2 were considered differentially expressed gene/transcripts. GO enrichment analysis provides all GO terms that significantly enriched in DEGs comparing to the genome background, and filter the DEGs that correspond to biological functions. All DEGs were mapped to GO terms in the Gene Ontology database(http://www.geneontology.org/), gene numbers were calculated for every term, significantly enriched GO terms in DEGs comparing to the genome background were defined by hypergeometric test. Pathway-based analysis helps to further understand

genes biological functions. KEGG is the major public pathway-related database. Pathway enrichment analysis identified significantly enriched metabolic pathways or signal transduction pathways in DEGs comparing with the whole genome background. Heatmap and volcano plot were drawn by the R package limma.

Cell culture and treatment

TUDCA (MCE, HY-19696) with different concentrations (1μM, 2μM, 5μM, 10μM, 20μM) was added in THP1 macrophages and RAW264.7 macrophages and the lipid storage were assessed by oil red o staining and dil-oxLDL uptake assay. Protein was extracted from the cells after 50 μg/mL oxLDL (Yiyuan Biotechnology, China) was added into the medium for 24 h and 10μM TUDCA treatment for another 24h. Negative control siRNA and siATF4 were transfected into RAW264.7 macrophages to inhibit ATF4. The most effective sequence of siATF4 was CCTCACTGGCGAGTGTAAA. Expression of ATF4 and AIM2 were analyzed by WB. Then RAW264.7 cells were transfected with negative control siRNA or AIM2 siRNA, which had AIM2 knockdown performed via Lipofectamine 3000 treatment for 24 h prior to stimulation. RAW264.7 macrophages were used for Oil Red O staining and the Dil-ox-LDL uptake assay (Yiyuan Biotechnology, China).

Oil Red O staining of cell

Foam cells and cross-sections of aortic sinuses were stained with Oil Red O for 30 min and then counterstained with haematoxylin. The lipid-stained areas of slides and cross-sections were observed and photographed using a microscope (Olympus), and the lipid droplet content was analysed using the Image Pro Plus image analysis soft-ware (version 6.0).

Dil-oxLDL uptake assay

The uptake of Dil-ox-LDL by RAW264.7 macrophage-derived foam cells was performed as previously described.[1] Briefly, RAW264.7 cell lines were transfected with siAIM2 and treated with TUDCA for 48h, washed twice with PBS, incubated with 10 μg/mL Dil-ox-LDL (Yiyuan Biotechnology, China) for 2 h at 37°C, and then washed and investigated via fluorescence microscopy.

Quantitative real time-PCR

Total RNA was extracted from the clinical samples and HCC cell lines using the RNAfast200 kit (Fastagen, Shanghai, China). The cDNA was synthesized using PrimeScripttmRT reagent Kit with gDNA Eraser (Takara, Shiga, Japan) according to manufacturer's instructions. Quantitative PCR was performed using FastStart Universal SYBR Green Master (Roche Diagnostic GmbH, Mannheim, Germany) on an Applied Roche LightCycler ® 480 II system, with the specific primers.

Western blot

All sample wells were loaded with 20ul of the protein mixture from mice or cells with separation using the gel apparatus (Bio-Rad) for 1 h at 120 V. Protein gels were blotted using the transfer apparatus and PVDF Midi transfer packs (Bio-Rad). Membranes were immediately transferred to a blocking buffer (5% Skim milk) for western blotting, and incubated with a gentle agitation for 1 h at room temperature. Membranes were cut horizontally and were incubated overnight with gentle agitation at 4°C in blocking buffer with a buffer containing primary antibodies (1:1000) which are listed in the manuscript. These blots were washed three times for 10 min in Tris-Buffered Saline with Tween-20 (TBST; 500 mM NaCl, 20 mM Tris–Cl, pH 7.5, 0.05 % (w/v) Tween 20), and incubated in a buffer containing corresponding secondary antibodies for 1 h with gentle agitation at room temperature. This was followed by three 10- min washes in TBST at room temperature and incubation in Clarity western ECL substrate chemiluminescent detection reagent (Millipore) for 5 min prior to image acquisition and exposure via Amersham Imager 600. For membrane strips of very close or overlapping molecular weight, antibody stripping buffer is used to wash the membrane for 30 minutes to wipe off the primary antibody and secondary antibody. Then followed by three 10-min washes in TBST at room temperature and incubation in another primary antibody, then these membranes were reprobed to get strip with close molecular weight.

QUANTIFICATION AND STATISTICAL ANALYSIS

Statistical analysis

Data analysis was performed using the GraphPad Prism 8·0 software (San Diego, CA, USA). All data were represented as mean $\pm$ standard deviation (SD). The differences between two groups were compared by unpaired Student's t-test. The differences among three or more groups were analyzed by one-way ANOVA followed by Tukey's multiple comparison test. All tests were two-tailed, and a value of $P < 0.05$ was considered to be statistically significant.

Code.R: Original code for analyzing the single cell RNA sequencing, related to the "scRNA sequencing analyses" in STAR Methods section.